LBL-29616
Preprint

Lawrence Berkeley Laboratory
UNIVERSITY OF CALIFORNIA

EARTH SCIENCES DIVISION

Submitted to Water Resources Research

Numerical Modeling of Steam Injection for the Removal of Nonaqueous Phase Liquids from the Subsurface. 2. Code Validation and Application

R.W. Falta, K. Pruess, I. Javandel, and P.A. Witherspoon

September 1990

Prepared for the U.S. Department of Energy under Contract Number DE-AC03-76SF00098.

DISCLAIMER

LBL-29616

Numerical Modeling of Steam Injection for the Removal of Nonaqueous Phase Liquids from the Subsurface 2. Code Validation and Application

R. W. Falta, K. Pruess, I. Javandel, and P. A. Witherspoon

Earth Sciences Division
Lawrence Berkeley Laboratory
University of California
Berkeley, California 94720

September 1990

This work was supported in part by the Director, Office of Energy Research, Office of Basic Energy Sciences, Engineering and Geosciences Division, and in part by the U.S. Environmental Protection Agency, under Interagency Agreement DW89931336-01-07, through U.S. Department of Energy Contract DE-AC03-76SF00098.

ABSTRACT

The multiphase steam injection simulator developed in part 1 [Falta et al., this issue] is used to simulate two laboratory column steam displacement experiments. In the first simulation, steam is injected into a clean, water saturated column, while in the second simulation, steam is injected into a column containing both water and separate phase trichloroethylene. In both cases, the numerical results are in good quantitative agreement with the experimental data. Based on the assumption of local chemical equilibrium between the phases, a simple criterion is derived for determining the major mechanism of NAPL/chemical transport during the steam displacement process. Several one-dimensional simulations of the steam displacement of high-boiling-point NAPLs are discussed. These results are consistent with theoretical predictions, and indicate that steam may efficiently displace organic liquids having boiling points substantially greater than that of water.

INTRODUCTION

Investigations at many hazardous waste sites have revealed the presence of nonaqueous phase liquids (NAPLs) in the subsurface. In many locations, hazardous organic liquids such as hydrocarbon fuels and chlorinated solvents have been stored in underground storage tanks. Experience has shown that as these tanks age, a significant number of them develop leaks. Often these leaks are difficult to detect, and result in the release of large amounts of hazardous NAPLs into the ground.

When lighter than water NAPLs are detected floating on the water table, an attempt is often made to remove the NAPL directly by means of wells or ditches. While large amounts of NAPL may be removed in this way, it is virtually impossible to remove all of the NAPL from the subsurface, and this technique does not address the problem of denser than water NAPLs. In light of these difficulties, it is often necessary to excavate the contaminated soils from a site. This method is expensive, and the excavated soil must be treated or disposed of as hazardous waste. For this reason, considerable emphasis is now being placed on developing remediation methods which may be performed in-situ. One promising method which has recently been proposed as an in-situ remediation technique is the sweeping of contaminated areas with steam [Hunt et al., 1988a,b; Udell and Stewart, 1989].

In part 1 [Falta et al., this issue], details of a numerical simulator developed for the purpose of modeling the steam remediation process were given. In this paper, the validation of the numerical simulator with one-dimensional steam injection experiments reported by Hunt et al. [1988b] is presented. In addition, a simple criterion is derived for the optimal removal of NAPLs by steam displacement as a function of

chemical and porous media characteristics. Finally, several simulations of the steam displacement of high boiling point NAPLs are discussed. The results of these simulations show the effect of specific NAPL chemical characteristics on the mechanisms of removal during steam sweeping.

SIMULATION OF LABORATORY COLUMN EXPERIMENTS

A series of laboratory-scale column steam injection experiments were conducted by Hunt et al. [1988b]. These experiments were designed to evaluate the mobilization and transport of a NAPL during water and steam flooding. A simplified diagram of the experimental geometry is shown in Figure 1. The experiments were conducted in a horizontal sand-packed glass column with a length of 91 cm and a diameter of 5.1 cm. The sand in the column had a size range of 160-200 μm, a porosity of 0.385, and a permeability of $1.6x\,10^{-11}m^2$. The column was instrumented with four ports connected to pressure transducers, and 22 ports containing thermocouples which projected into the column centerline. An additional port was used to inject NAPL into the column centerline. The column was wrapped with heater tapes, and insulated with about 7.6 cm of insulation. The power to each of the heater tapes during the experiments was calibrated to minimize radial heat losses, and to maintain one-dimensional heat flow in the column. Further details of the experimental apparatus are given by Hunt et al. [1988b].

A total of four experiments were conducted. In the first experiment, referred to as the baseline experiment, steam was injected at a rate of $3.534x\,10^{-5}$ kg/s into the water-saturated column until steam breakthrough at the outlet occurred. In the

remaining three experiments, 18 ml of a NAPL was injected into the column centerline 27 cm from the column inlet. In these three experiments, three different NAPLs were used: trichloroethylene (TCE), an equal volume mixture of benzene and toluene, and regular unleaded gasoline.

During the three experiments involving a NAPL, the following procedure was used. First, the NAPL was injected into the centerline of the water saturated column. This was followed by cold water injection at a Darcy velocity of 15 m/day for several pore volumes. The flowrate was then lowered to a Darcy velocity of 1.5 m/day prior to the steam injection. Steam was then injected into the column at a mass rate of $3.534x\,10^{-5}$ kg/s until some time after steam breakthrough at the outlet occurred. The water mass flowrate used during the steam injection part of the experiments was equal to that used during the 1.5 m/day waterflood part of the experiments. Although the injected steam quality, X, (defined as the ratio of the mass of water vapor to the total water mass) was not measured directly, the value was calculated by Hunt et al. [1988b] to be about 0.44 for the baseline experiment, 0.49 for the TCE displacement experiment, and 0.52 for the benzene/toluene displacement experiment. Additional details of the experimental procedure may be found in Hunt et al. [1988b]. Analytical and semi-analytical solutions which were used to model these experiments are given by Hunt et al. [1988a] and Stewart and Udell [1988].

For the purpose of validating the STMVOC simulator, the baseline and the TCE displacement experiments were modeled numerically. Because the STMVOC simulator does not account for multicomponent NAPL effects, no attempt was made to model the benzene/toluene or the gasoline displacement experiments.

Simulation of Baseline Steam Injection Experiment

The baseline steam injection experiment was simulated using the multiphase STMVOC code. A one-dimensional mesh consisting of 50 uniformly spaced elements with a mesh spacing of 1.82 cm was used for the simulations. The values of material properties needed in the simulation were taken from Hunt et al. [1988a,b], and are listed in Table 1.

The partially saturated porous media thermal conductivity, λ, is computed using a parallel type conduction model as

$$\lambda = \lambda_D + S_w(\lambda_W - \lambda_D) \tag{1}$$

with

$$\lambda_D = \lambda_W - \phi\lambda_w$$

where λ_D is the dry porous media thermal conductivity, λ_W is the water saturated porous media thermal conductivity, and λ_w is the thermal conductivity of liquid water (about 0.61 $W/m\ ^oC$). The value of the water saturated thermal conductivity of 3.1 $W/m\ ^oC$ was suggested by Hunt et al. [1988b].

The relative permeability and capillary pressure curves used in the simulation are summarized in Table 2. Hunt et al. [1988b] did not measure the relative permeabilities or the capillary pressure of the sand pack as a function of saturation, although they estimated that the gas phase relative permeability has a value of 0.4 at a gas saturation of 0.75. Because no direct measurements of relative permeability or capillary pressure for this sand pack were available, the choice of these particular curves is somewhat arbitrary. The relative permeability curves used in the

simulation are similar in form to those suggested by Frick [1962] for unconsolidated, well sorted sands, and the gas phase relative permeability has a value of 0.42 at a gas saturation of 0.75.

The gas-water capillary pressure function given in Table 2 is the widely used van Genuchten [1980] formulation. The values of the constants α_{gw}, n, and S_m used in this equation were reported by Parker et al. [1987], and are based on measurements made in a sandy porous media.

The initial conditions for the simulation are an initial water saturation of 0.995 (a gas saturation of 0.005), an initial temperature of 22 ^oC, and an initial pressure of 101.3 kPa (one atmosphere). At the inlet end of the column, the boundary condition is a water mass injection rate of $3.534x10^{-5}$ kg/s with a specific enthalpy of 419 kJ/kg during the first 468 s of steam injection, and a specific enthalpy of 1562 kJ/kg thereafter. The water specific enthalpy of 419 kJ/kg corresponds to liquid water at a temperature of 100 ^oC. This value was based on the observation of Hunt et al. [1988b] that 468 s were required for the steam to heat the inlet plate before steam began to enter the sandpack. The steam specific enthalpy of 1562 kJ/kg is representative of steam with a quality of 0.5 and a temperature of 105 ^oC. This steam quality is an approximate average of the steam quality values reported by Hunt et al. [1988b] for the different experiments.

At the outlet, a deliverability model using a constant outlet pressure was used as the boundary condition. With this boundary condition, the production rate of phase β is

$$q_\beta = \frac{k_{r\beta}}{\mu_\beta} PI \cdot (P_\beta - P_{wb}) \qquad (2)$$

where P_β is the pressure of phase β at the center of the producing element, P_{wb} is the specified outlet pressure, $k_{r\beta}$ is the β phase relative permeability in the element, and μ_β is the β phase viscosity in the element. The productivity index, PI, is calculated from

$$PI = \frac{kA}{D} \tag{3}$$

where k is the permeability, A is the column cross-sectional area, and D is the distance from the center of the outermost element to the outer boundary (0.91 cm). The outlet pressure, P_{wb}, was assigned a value of 101.4 kPa. If the pressure at the center of the producing element is less than the specified outlet pressure, the production rate is zero (no backflow). Using (2), the rate of heat removal is calculated as

$$q^h = \sum_\beta q_\beta h_\beta \tag{4}$$

where h_β is the specific enthalpy of the β phase. Similarly, the rate of removal of each mass component, K, is

$$q^K = \sum_\beta q_\beta \omega_\beta^K \tag{5}$$

where ω_β^K is the mass fraction of component K in phase β. For this problem, only two mass components are used, water and a small amount of air.

During the simulation, the timestep size was allowed to vary according to the rate of convergence of the Newton-Raphson iterative solution. When convergence was obtained in 4 iterations or less, the timestep size was doubled. If convergence was not achieved in 9 iterations, the timestep size was reduced by a factor of 4, and a new iteration process was started. From the start of steam injection until steam

breakthrough at the outlet, a total of 320 timesteps were used with an average timestep size of 20.8 s. Following steam breakthrough at the outlet, the timestep size becomes much larger as the system approaches steady state.

Figure 2 shows the simulated temperature and water phase saturation profiles 3000 s after the start of steam injection. At this time, the steam condensation front is located about 35 cm from the inlet. Behind the steam front, the temperature profile is nearly linear with distance, and is determined by the gas pressure distribution under saturated vapor conditions. Ahead of the steam front, the temperature decays exponentially with distance in accordance to the theory presented by Hunt et al. [1988a].

Far behind the steam front, the water saturation has a nearly constant value of 0.30. This is slightly different from the approximate value calculated by Hunt et al. [1988b] of 0.25. The difference in these values is probably due to the particular choice of relative permeability and capillary curves used in the simulation. Closer to the steam condensation front, the water saturation increases rapidly, and ahead of the steam front the column is fully water saturated. In Figure 2, the small gas saturation just ahead of the steam front is due to the initial condition of $S_w = 0.995$. During the steamflood, the small amount of air initially present in the column becomes concentrated just ahead of the steam front. If the column initially contained no air, this small gas saturation ahead of the steam front would not be present.

From Figure 2, it is clear that in the vicinity of the steam condensation front, major changes in the temperature and water saturation occur over very small distances. Because transport parameters such as relative permeabilities and viscosities

are strong, nonlinear functions of saturation and temperature respectively, major nonlinearities in the governing equations occur.

A comparison of the experimentally measured and the numerically calculated steam condensation front locations is shown in Figure 3. The numerical results are in excellent agreement with the experimental data.

In Figure 4, the calculated temperature profile 3000 s after the start of steam injection is compared with the experimentally determined profile. In this figure, the experimental temperature profile was constructed by using the experimental steam front location shown in Figure 3 along with the average experimental temperature profile ahead of the steam front given in Hunt et al. [1988b]. The calculated temperature profile is in good agreement with the experimental profile, although some numerical smearing of the sharp temperature front is evident. Numerical simulations using a very fine mesh resulted in somewhat better agreement with the experimental data, but at a cost of greatly increased computational effort.

Due to the rapid changes in nonlinear parameters such as the relative permeabilities, viscosities, and water vapor pressure which occur in an element as the steam front passes through, it is necessary to use small timesteps in order to achieve convergence. For this problem, about 6 timesteps were required to simulate the propagation of the steam front through each element. This number of timesteps was found to be relatively insensitive to the size of the elements. For this reason, reducing the size of the elements by a factor of 2 (doubling the number of elements) doubles the number of timesteps needed to simulate the problem. Because doubling the number of elements more than doubles the number of computations needed for each timestep,

the net result of decreasing the element size by a factor of 2 is an increase in the cpu time by a factor of more than 4.

During the numerical simulation of an advancing steam front in a porous medium, the steam front tends to move in a series of jumps due to the finite spatial discretization. As the steam front approaches an element, hot water begins to enter the element, and the temperature in the element begins to rise. During this period, the water saturation remains constant (fully saturated). Heating of the element continues until the temperature approaches the water boiling temperature. When the temperature of the element reaches the water boiling temperature, the water saturation in the element suddenly drops as the steam front enters the element. Typically, the water saturation in an element that has just reached the water boiling temperature will drop from about 0.95 to about 0.6 in two timesteps. As the next downstream element begins to approach the steam temperature, the process is repeated. If it were possible to use a mesh with an infinitesimal spacing, the steam front would advance smoothly through the system. The use of finite mesh spacing results in a spurious cyclical variation in pressure and flowrates as the steam front advances into each element.

This effect is well known, and is discussed in some detail by Pruess et al. [1987]. While the pressures and flowrates calculated at each timestep show a characteristic oscillation, if these values are averaged over the time required for the steam front to advance one element, the results are good.

In Figure 5, the calculated pressure gradient between the first two pressure ports located 13.5 and 35.4 cm from the inlet is shown. The thin line is a plot of the

calculated pressure gradients at every timestep. As discussed above, these results show a cyclical variation with a frequency corresponding to the movement of the steam front across each element. The darker line was calculated by taking a weighted average of the pressure gradient over each cycle. The pressure gradient shown in this figure is the gas phase pressure gradient. Because the capillary pressure function given in Table 2 tends towards zero as the gas saturation becomes small, the calculated gas and water pressures become equivalent at low gas saturations.

The averaged calculated pressure gradient shown in Figure 5 is compared with the experimental data of Hunt et al. [1988b] in Figure 6. As explained by Hunt et al. [1988b], the pressure gradient data reflects three distinct flow conditions. The early part of the curve, from 0 to about 0.15 displaced pore volumes is indicative of single phase liquid water flow between the pressure ports. At this point, the steam front has not yet reached the first pressure port, and both pressures are measured in the water phase.

The center part of the curve, from about 0.15 to about 0.50 displaced pore volumes reflects multiphase flow between the pressure ports. The large rise in the pressure gradient from about 0.15 to about 0.2 displaced pore volumes occurs as the steam front passes by the first pressure port. As the front passes the pressure port, the pressure measured in the port switches from the water phase to the gas phase [Hunt et al., 1988b]. The rapid rise in the pressure gradient at this time is due to the capillary pressure difference between the two phases. As the water phase saturation at the first pressure port drops, the capillary pressure increases.

From about 0.2 to about 0.4 displaced pore volumes, the pressure gradient continues to increase as a high velocity steam zone (with a large pressure drop) develops between the pressure ports. During this period, the capillary pressure increases by only a small amount as the water saturation at the first pressure port becomes nearly constant. At about 0.4 displaced pore volumes, the steam front passes by the second pressure port, and the capillary pressure gradient between the ports rapidly diminishes.

In the final part of the curve, from about 0.5 to 1.0 displaced pore volumes, the pressure gradient becomes nearly constant at a value of about 25 kPa/m, and is representative of single phase high velocity steam flow between the pressure ports. The calculated pressure gradients shown in Figure 6 reflect the different flow conditions discussed above, and approximately match the experimental data. It is significant to note that this match of the experimental data was achieved without calibrating any of the various parameters.

Figure 7 shows a comparison of the calculated and experimentally determined cumulative liquid volume displaced from the column as a function of the injected liquid volume. These liquid volumes are calculated from the mass flow rates, and are given as equivalent liquid volumes at the ambient (22 ^{o}C) temperature. The plotted results show three different conditions during the steam flood. In the early part of the steam injection, all of the steam entering the column condenses. As a result, the entire column is water saturated, and the volume of liquid water produced is equal to the equivalent volume injected. Under these conditions, the curve shown in Figure 7 would be expected to be linear with a slope of 1.

As the steam front begins to propagate through the column, the liquid volume produced becomes larger than the equivalent liquid volume injected due to the displacement of the original liquid. For an injected mass flux of $\dot{m}_{in}^{w}$, the produced mass flux, $\dot{m}_{pro}^{w}$ is approximately [Hunt et al., 1988a]

$$\dot{m}_{pro}^{w} = \dot{m}_{in}^{w} + \rho_w \phi V_{sf} (1 - \bar{S}_w) \tag{6}$$

where V_{sf} is the steam front velocity, ρ_w is the water phase density, ϕ is the porosity, and $\bar{S}_w$ is the average water saturation behind the steam front. For the experimental conditions considered here, the ratio of the produced mass flux to the injected mass flux is about 3.3. The numerically calculated and experimentally determined curves shown in Figure 7 reflect this enhanced displacement, and have a slope of about 3.3.

As the steam breaks through at the end of the column, the initial pore water is no longer displaced, and the produced mass flux becomes equal to the injected mass flux. In Figure 7, this is seen to occur after the production of about 1.06 pore volumes for the experimental curve. The calculated steam breakthrough occurs somewhat sooner, after about 1.02 produced pore volumes. This difference is due to the fact that in the simulation, the average water saturation after steam breakthrough is about 0.30 compared to the experimental value of about 0.25. Because the water saturation behind the steam front is determined in large part by the water phase relative permeability and capillary pressure, by calibrating the curves used in the simulation, better agreement could be obtained.

Simulation of the Trichloroethylene Displacement Experiment

The TCE displacement experiment was modeled with the STMVOC simulator using the same mesh that was used for the baseline steam injection simulations. The porous medium material properties used in the simulation are identical to those used in the baseline simulation (see Table 1) except that the thermal conductivity expression given by (1) was modified to include the effects of the NAPL. Using a parallel type conduction model, the porous media thermal conductivity is

$$\lambda = \lambda_D + S_w(\lambda_W - \lambda_D) + \phi S_n \lambda_n \tag{7}$$

where λ_n is the NAPL thermal conductivity, and S_n is the NAPL saturation.

The thermophysical properties of TCE are calculated internally by the STMVOC simulator as functions of pressure, temperature, and composition. A detailed description of the methods used to compute various NAPL/chemical properties was presented in part 1 [Falta et al., this issue]. In Table 3, a complete listing of the constants used by STMVOC to calculate the properties of TCE is given. The majority of this data may be found in Reid et al. [1987]. Because the TCE displacement experiment was conducted in a clean sand, the fraction of organic carbon in the sand was assumed to be zero, and adsorption of TCE to the solid phase was neglected.

The relative permeability and capillary pressure curves used in the TCE simulation are similar to those used for the baseline simulation, and are listed in Table 4. The gas and water phase relative permeability functions are identical to those used in the baseline simulation. The NAPL phase relative permeability is calculated using

the three phase method of Stone [1970] with the modifications suggested by Aziz and Settari [1979]. The binary gas-NAPL and water-NAPL relative permeabilities needed for the three phase NAPL relative permeability are similar to functions suggested by Frick [1962] for unconsolidated, well sorted sands. The residual NAPL saturation (below which separate phase TCE flow cannot occur) was assumed to be 0.05.

The gas-NAPL and gas-water capillary pressure functions shown in Table 4 are modified versions of the van Genuchten [1980] equation given by Parker et al. [1987]. The values of the constants α_{gn}, α_{nw}, n, and S_m used in the capillary pressure functions are given by Parker et al. [1987], and are based on experiments conducted in a sandy porous medium. As the NAPL saturation tends towards zero, the three phase capillary pressure formulation reduces exactly to the two phase formulation used in the baseline steam injection simulation.

Because the TCE displacement experiment conducted by Hunt et al. [1988b] involved several different experimental conditions, several different boundary conditions were required in the simulation. The initial conditions for the simulation are the same as before, a water saturation of 0.995, a temperature of 22 ^oC, and a pressure of 101.3 kPa. The NAPL injection part of the experiment is simulated by using the 15th element from the inlet as a source element. The center of this element is located 26.4 cm from the column inlet. Over a period of 120 s, TCE is injected into this element at a rate of 2.19×10^{-4} kg/s. This corresponds to a total of 18 ml of liquid TCE. The specific enthalpy of the injected TCE is equal to that of liquid TCE at 22 ^oC. During this part of the simulation, deliverability boundary conditions are

used at either end of the column (see (2)-(5)) with the inlet and outlet pressures constant at 101.4 kPa.

Following the simulation of the NAPL injection part of the experiment, the inlet boundary condition is switched to a specified water mass injection rate with a given specific enthalpy. During the high speed waterflood, the water mass injection rate is $3.534x\,10^{-4}$ kg/s with a specific enthalpy of 92.3 kJ/kg. This corresponds to a Darcy velocity of 15 m/d in the column with an injection temperature of 22 ^{o}C. As in the experiment, after 9.5 pore volumes of water have been produced from the column, the water injection rate was lowered to $3.534x\,10^{-5}$ kg/s, corresponding to a Darcy velocity of 1.5 m/d. This rate is maintained until a total of 12.5 pore volumes of water have been removed from the column. During the simulation of the waterflood, the deliverability boundary condition with an outlet pressure of 101.4 kPa was used at the column outlet. Under this boundary condition, the total TCE removal rate is the sum of the TCE removal rate in all phases, and may include dissolved TCE in the aqueous phase, TCE vapor in the gas phase, and separate phase TCE. During the simulation of the waterflood part of the experiment, TCE removal from the column was observed to occur only in the form of dissolved TCE in the aqueous phase. This is consistent with the experimental observations of Hunt et al. [1988b].

In Figure 8, the simulated separate phase TCE (NAPL) distribution during the waterflood is shown. Immediately following the TCE injection, the TCE is present at high saturations over a very narrow length of the column. During the early part of the high speed waterflood, the separate phase TCE begins to spread downstream. Eventually, the separate phase TCE becomes distributed over about a third of the

column at a phase saturation of slightly over the NAPL residual saturation of 0.05. During the waterflood, the upstream edge of the separate phase TCE dissolves into the water and is carried downstream. Because TCE has a relatively high solubility in water of 1.1 g/l, during the waterflood, about a third of the injected TCE is dissolved in the water and removed from the column.

At the end of the waterflood, the inlet boundary conditions are switched to the steam injection conditions used in the baseline simulation. A water mass injection rate of $3.534x10^{-5}$ kg/s with a specific enthalpy of 419 kJ/kg is used during the first 468 s of the steam injection to simulate the heating of the column inlet plate. After this period, the specific enthalpy is raised to 1562 kJ/kg, corresponding to steam with a quality of 0.5 and a temperature of 105 ^{o}C. During the steam injection part of the simulation, the deliverability boundary condition is used at the outlet with an outlet pressure of 101.4 kPa. A total of 470 timesteps were used to simulate the steam injection part of the simulation with an average timestep length of 14.0 s. This average timestep length is somewhat smaller than the average timestep size used during the baseline simulation of 20.8 s. This is due to the added nonlinearity and coupling which occurs during three-phase flow with a rapid phase change in two of the three phases compared with two-phase flow with a rapid phase change in only one phase.

Figure 9 shows the simulated separate phase TCE saturation after the waterflood, and the temperature profile and TCE separate phase saturation during the steamflood. As mentioned earlier, towards the end of the waterflood, the separate phase TCE was distributed over about a third of the column at a saturation of

slightly more than 0.05. At this point, the separate phase TCE is nearly immobile, and transport of the TCE component in the column is by dissolution of the upstream edge of the NAPL with subsequent advection with the flowing water.

When steam is injected into the column and the steam condensation front reaches the zone containing the TCE, the TCE is very efficiently mobilized. As the steam front propagates through the column, the separate phase TCE (which has a normal boiling point of 87.3 ^{o}C) forms a sharp NAPL bank just ahead of the steam condensation front. In the narrow zone occupied by the TCE, transport of the TCE occurs primarily due to advection in the gas phase and separate phase TCE flow. As the upstream edge of the TCE boils and evaporates, it is carried ahead by the gas phase to a cooler part of the column where it condenses. Due to the rapid drop in temperature ahead of the steam condensation front, and the strong dependence of TCE vapor pressure on temperature, the region in which TCE boiling, evaporation, and condensation occurs tends to be very small. This results in an increase in the separate phase TCE saturation to a value greater than the residual saturation. As a result of this increased NAPL saturation and the decreased TCE liquid viscosity at the higher temperatures, separate phase TCE flow is facilitated.

The temperature profile shown in Figure 9 is similar to the profile calculated for the baseline case, and is in fair agreement with the experimental profile although some smearing of the sharp front is evident. In Figure 10, the calculated steam condensation front location in time is compared with the experimental data. The numerical result is in good agreement with the experimental data although the calculated position is shifted somewhat with respect to the experimental data. This is due to

the fact that the time required for heating the inlet plate in the experiment was not exactly matched by the boundary conditions during the simulation.

The averaged calculated pressure gradient over the first two pressure ports is compared with the experimental data in Figure 11. As in the case of the baseline simulation, the calculated pressure gradient data at each timestep have a cyclical variation over the time required for the steam front to advance one element. The averaged pressure gradient (averaged over the time required for the steam front to advance by one element) is in good agreement with the experimental data, and reflects the complex multiphase flow conditions which evolve over the course of the steam injection. The calculated curve is shifted slightly from the experimental curve due to the small error in matching the experimental end effects as discussed above.

A comparison of the calculated and experimentally determined cumulative total liquid volume displaced from the column (including TCE) as a function of the injected liquid volume is shown in Figure 12. The volumes are calculated from mass flow rates and are reported as equivalent liquid volumes at ambient conditions. As in the earlier comparison shown for the baseline case in Figure 7, the calculated curve closely matches the experimental data, and shows the characteristic changes of slope which result from different flow conditions in the column. As in the baseline simulation, in the TCE simulation, the water saturation behind the steam front is slightly overestimated due to the choice of relative permeability and capillary pressure curves.

In Figure 13, the measured and calculated cumulative volume of TCE removed from the column during the experiment is shown. This volume is calculated from

the TCE mass flows at the outlet converted to equivalent liquid TCE volume at ambient conditions. Prior to steam injection at 12.5 displaced pore volumes, TCE was removed from the column by dissolution and advection in the aqueous phase only. Hunt et al. [1988b] report that the concentration of TCE in the water leaving the column was at the TCE solubility limit. After about one pore volume of liquid was displaced by the steam injection, and just before steam breakthrough at the outlet, separate phase TCE was produced. The numerically calculated result is in good agreement with the experimental data.

The calculated volume of TCE removed in each phase is shown in Figure 14. During the waterflood and the early part of the steamflood, before steam breakthrough, a total of 6.94 ml of TCE is removed from the column in the form of dissolved TCE. Immediately before steam breakthrough, 9.70 ml of TCE is produced over a short period of time as a separate phase. The remaining 1.36 ml of TCE is produced as TCE vapor immediately following the steam breakthrough. After 1.82 hours of steam injection, the results of the numerical simulations indicate that all of the TCE has been removed from the column. This is consistent with the experimental observations of Hunt et al. [1988b], although they report that a small amount of TCE was found trapped in the pressure ports at the end of the experiment.

In order to assess the importance of TCE vapor diffusion on the steam displacement process, the TCE displacement simulation was repeated without diffusion. A comparison of the results of these simulations shows that the diffusion of TCE vapors has little effect on the one-dimensional steam displacement process. This is due to the very high rate of gas phase advection of TCE near the steam front. This

strong advection completely dominates the gas phase transport of TCE.

A CRITERION FOR OPTIMAL NAPL REMOVAL BY STEAM INJECTION

If a NAPL is present in a porous medium at a phase saturation less than or equal to the NAPL residual saturation (S_{nr}), the NAPL is immobile. When the NAPL is immobile, the only mechanisms for NAPL removal involve the interphase mass transfer of the chemical component from the NAPL into either the gas phase or the aqueous phase. The interphase mass transfer of the chemical from the NAPL to the gas phase occurs due to boiling or evaporation of the NAPL, while the interphase mass transfer of the chemical from the NAPL to the aqueous phase occurs due to dissolution of the NAPL. The type and magnitude of interphase mass transfer of the chemical from the NAPL is highly dependent on the multiphase flow conditions, and on the chemical characteristics of the NAPL/chemical.

In a one-dimensional system, the process of steam displacement for the removal of a NAPL from a porous medium may be described as an optimal process if the NAPL is completely displaced by the advancing steam front. With this definition, during an optimal steam treatment, none of the NAPL would remain in the steam zone behind the steam condensation front. During an optimal steam treatment, almost all of the NAPL/chemical would be produced from the system immediately before steam breakthrough at the producing location. Following the steam breakthrough, the amount of NAPL/chemical produced would be small, and steam injection could be discontinued shortly after steam breakthrough. The TCE displacement experiment discussed earlier would be an example of an optimal steam treatment.

Naturally, in a field application it would also be necessary to have good sweep of the contaminated area by the steam in order for the treatment to be efficient.

From the definition of an optimal steam displacement, it follows that a less than optimal steam displacement process is one in which a certain amount of the NAPL remains in the steam zone behind the steam condensation front. Under these conditions, the NAPL/chemical would not necessarily be produced in large amounts prior to steam breakthrough at the producing location. In this case, the NAPL/chemical would continue to be produced at a low rate following the steam breakthrough, and steam injection would have to continue for some time in order for complete NAPL removal to be achieved.

It should be mentioned here that the characterization of a steam displacement process as less than optimal does not necessarily mean that steam treatment would not be an effective treatment method. Even though the NAPL would not be produced as a separate phase ahead of the steam condensation front, the removal of the NAPL would still be greatly enhanced compared to ordinary isothermal treatment methods. This is due to the fact that the saturated vapor pressure of most NAPLs at $100^{o}C$ is often two or more orders of magnitude larger than the saturated vapor pressure at $20^{o}C$. This increase in the saturated vapor pressure results in a proportional increase in the rate of evaporation of a NAPL for a given gas flowrate through the contaminated zone.

By examining the steam displacement process in an idealized system, it is possible to develop a necessary condition for the optimal removal of a NAPL by steam treatment. Consider a one-dimensional porous medium which initially contains a

NAPL at a saturation greater than or equal to the residual saturation for the NAPL in the medium. It is assumed that all of the NAPL present at a saturation greater than the residual saturation will be displaced as a separate phase ahead of the advancing steam front by viscous forces. This is a strong assumption, and the degree to which the NAPL will be displaced as a separate phase ahead of the steam front depends on several factors. Stewart and Udell [1988] present a theoretical evaluation of the mechanisms of NAPL displacement as a separate phase during steam injection. They conclude that the ratio of NAPL to water viscosity is the leading factor which determines the separate phase NAPL displacement by viscous forces. The assumption that the NAPL saturation will be reduced to the residual saturation by separate phase flow due to viscous forces represents a favorable condition for the separate phase NAPL displacement ahead of the steam front (ie. low NAPL viscosity). For this reason, the following criterion is a necessary but not sufficient condition for optimal NAPL removal.

Because the residual saturation of NAPL is immobile, as the steam front advances, the NAPL can only be removed by interphase mass transfer. Obviously, if the NAPL boiling point is less than that of water, the NAPL will be completely vaporized at the steam front, and the NAPL removal will be efficient. The interphase mass transfer of higher boiling point NAPLs is dominated by evaporation behind the steam condensation front due to the characteristically low water solubilities of NAPLs. In the absence of significant dissolution, the condition for optimal NAPL removal is that the rate of NAPL evaporation behind the steam condensation front must be large enough so that the speed of the evaporation front through a

residual saturation of NAPL is greater than the speed of the advancing steam front. It should be noted that this condition does not consider the effects of adsorption of the chemical onto solid particles, an effect which could be important in some cases. For an evaporation front velocity of V_{evf}, and a steam front velocity of V_{sf}, this condition may be written as

$$V_{evf} > V_{sf} \tag{8}$$

or

$$\frac{V_{evf}}{V_{sf}} > 1 \tag{9}$$

The evaporation front velocity is determined by the rate of evaporation per unit cross sectional area, E, divided by the mass of NAPL per unit porous medium volume, M_n. The evaporation front velocity is then

$$V_{evf} = \frac{E}{M_n} \tag{10}$$

If the evaporating NAPL is in local chemical and thermal equilibrium with the gas phase, the evaporation rate may be written as

$$E = V_s \bar{C}_g^c \tag{11}$$

where V_s is the steam Darcy velocity behind the steam front (not to be confused with the steam front velocity), and $\bar{C}_g^c$ is the saturated vapor concentration of the evaporating chemical at the steam temperature. From a simple mass balance, the maximum steam Darcy velocity behind the steam condensation front is

$$V_s = \frac{\dot{m}_{in}^w X}{\rho_s} \tag{12}$$

where $\dot{m}_{in}^{w}$ is the injected water mass flux, X is the injected steam quality, and ρ_s is the density of the steam. Because the magnitude of the steam quality decreases as the steam condensation front is approached, the use of the injected steam quality in (12) will tend to overestimate the steam Darcy velocity near the steam condensation front. The use of this value in the calculation of the evaporation rate gives an optimistic estimate of the evaporation velocity. This is in keeping with the earlier assumption of favorable separate phase NAPL displacement ahead of the steam front, and helps ensure that the condition given by (9) is a minimum requirement for optimal NAPL removal. The assumption of local equilibrium between the NAPL and gas phase has a similar effect because it results in a maximum rate of interphase mass transfer. By assuming ideal gas behavior, the saturated vapor concentration of the evaporating chemical may be calculated by

$$\bar{C}_g^c = \frac{P_{sat}^c M_{wt}^c}{RT_s} \tag{13}$$

where P_{sat}^c is the saturated vapor pressure of the NAPL at the steam temperature, T_s, and M_{wt}^c is the molecular weight of the NAPL. The use of (13) instead of the real gas law is a reasonable approximation as long as the vapor pressure is not more than a few atmospheres.

For a residual NAPL saturation, the mass of NAPL per unit porous medium volume is

$$M_n = \phi \rho_n S_{nr} \tag{14}$$

where ρ_n is the NAPL density at the steam temperature. Combining (12), (13), and (14), the maximum evaporation front velocity is

$$V_{evf} = \frac{\left[\frac{\dot{m}_{in}^{w} X}{\rho_s}\right]\left[\frac{P_{sat}^{c} M_{wt}^{c}}{RT_s}\right]}{\phi \rho_n S_{nr}} \tag{15}$$

From (15), it is apparent that for given steam injection conditions, the evaporation front velocity increases with increasing NAPL saturated vapor pressure, and decreases with increasing NAPL residual saturation.

For a one-dimensional steamflood, Menegus and Udell [1985] derived an analytical solution for the steady-state steam condensation front velocity. This expression, which does not include the thermodynamic effects of a NAPL, is written as

$$V_{sf} = \frac{\dot{m}_{in}^{w}}{\rho_w} \frac{\frac{X h_{vap}^{w}}{C_w (T_s - T_o)} + 1}{(1-\phi)\frac{\rho_R C_R}{\rho_w C_w} + \phi \bar{S}_w} \tag{16}$$

where h_{vap}^{w} is the water heat of vaporization, C_w is the liquid water heat capacity, T_s is the temperature of the steam zone, T_o is the ambient (initial) temperature, and $\bar{S}_w$ is the water phase saturation in the steam zone well behind the steam condensation front. Although the effects of a NAPL are neglected in (16), NAPLs typically have a low heat of vaporization compared to water, and the error incurred by using (16) to estimate the steam front velocity in a system in which a NAPL is present at low saturations is probably small.

In Table 5, the ratio of evaporation front velocity to steam condensation front velocity is given for three high boiling point NAPLs for conditions similar to the experimental conditions used by Hunt et al. [1988b]. The steam condensation front

velocity was calculated using (16) with $\dot{m}_{in}^{w}$=1.73x10^{-2} kg/m^2s, X =0.5, h_{vap}^{w}=2257 kJ/kg, C_w=4.21 kJ/kg^oC, T_s=100 ^oC, T_o=20 ^oC, ρ_w= 1000 kg/m^3, and $\bar{S}_w$=0.3. The remaining parameter values used in (16) are given in Table 1. For the given parameter values, the steam condensation front velocity calculated by (16) is 12.9 m/day. This velocity is within the range of steam front velocities reported by Hunt et al. [1988b] for the different steam injection experiments.

The evaporation front velocities for the three NAPLs in Table 5 were calculated using (15) with S_{nr}=0.05, ρ_s=0.6 kg/m^3, and T=100 ^oC. The evaporation front velocity for n-decane was also calculated for a NAPL residual saturation (S_{nr}) of 0.25. The NAPL vapor pressure, P_{sat}^{c}, and density, ρ_n were calculated using (23) and (34) from part 1 [Falta et al., this issue], respectively. For the conditions discussed above, the maximum steam velocity behind the steam condensation front is calculated to be about 1246 m/day. Because the three NAPLs examined in Table 5 have substantially different chemical properties, the calculated evaporation front velocities vary over a wide range.

The aromatic hydrocarbon, o-xylene, with a normal boiling point of 144.5 ^oC has a fairly high saturated vapor concentration at the steam temperature. This large saturated vapor concentration, in combination with the very high steam velocity behind the steam front results in a calculated evaporation front velocity which is 5.6 times faster than the steam condensation front velocity for a residual saturation equal to 0.05. Since the ratio of these velocities is greater than one, the calculations presented in Table 5 suggest that the steam displacement of xylene would be an optimal process even though the boiling point of xylene is substantially higher than

that of water. This behavior has been experimentally verified by a laboratory scale steam displacement experiment in which xylene was effectively removed from the system (K. S. Udell, personal communication, 1989).

The aliphatic hydrocarbon n-decane has a much higher boiling point than water, 174.2 ^{o}C, and it would seem unlikely that such a NAPL would be effectively removed by a low pressure steamflood. However, n-decane has a significant saturated vapor pressure at 100 ^{o}C, resulting in a moderately large saturated vapor concentration at that temperature. For a residual saturation of 0.05, the calculated ratio of evaporation front velocity to steam condensation front velocity is 3.3, implying that n-decane could be effectively removed by steam injection. However, when the NAPL residual saturation is increased to a value of 0.25, the ratio of the evaporation front velocity to the steam condensation front velocity decreases to 0.7. Since this value is less than one, it is anticipated that the n-decane displacement in this case would be less than optimal, and the n-decane would not be displaced as a separate phase ahead of the steam front.

The polycyclic aromatic hydrocarbon 1-methylnapthalene has a very high boiling point, 244.8 ^{o}C. The saturated vapor pressure of 1-methylnapthalene is very small, even at 100 ^{o}C. For this reason, the saturated vapor concentration and evaporation front velocity are also small, and the ratio of the evaporation front velocity to the steam condensation front velocity for a NAPL residual saturation of 0.05 is only 0.2. Since this value is much smaller than one, it is expected that the removal of 1-methylnapthalene by low pressure steam would not be optimal, and that 1-methylnapthalene would not be displaced as a separate phase ahead of the steam

front. Stewart and Udell [1988] report that during a column steam displacement experiment using a high-viscosity, nonvolatile oil, the oil was not produced as a separate phase ahead of the steam front. Because this oil is less volatile than 1-methylnapthalene, it is likely that the necessary condition given by (9) is not satisfied, and this behavior is to be expected.

To further illustrate the behavior of high boiling point NAPLs during steam injection, a series of numerical simulations were conducted. These simulations were performed using the same geometry and boundary conditions as in the TCE displacement simulation, but with o-xylene, n-decane, and 1-methylnapthalene as the NAPL. In each case, 18.0 ml of the NAPL was injected into the column followed by cold water injection and then steam injection. The constants used by the STMVOC simulator to compute the thermophysical properties of these three NAPLs are listed in Table 6. The material properties and relative permeability and capillary pressure curves used in these simulations are identical to those used in the TCE displacement simulation except that one simulation was performed using n-decane with $S_{nr} = 0.25$.

In Figure 15, the simulated separate phase o-xylene saturation after the waterflood, and the temperature profile and o-xylene separate phase saturation during the steamflood are shown. These results were computed using $S_{nr} = 0.05$. From this figure, it is clear that the o-xylene is completely mobilized during the steamflood, forming a NAPL bank ahead of the advancing steam front. The removal of the o-xylene from the column is similar to the TCE removal except that a smaller amount of o-xylene is removed as a dissolved species in the aqueous phase. This is due to the lower solubility (175 mg/l) of xylene compared to TCE (1100 mg/l).

Figure 16 shows the calculated separate phase distribution of n-decane after the water flood, and the temperature profile and separate phase n-decane distribution during the steamflood. Again, S_{nr} was set equal to 0.05. The results are nearly identical to the xylene case, and the decane forms a NAPL bank just ahead of the steam condensation front. The removal of decane from the column is similar to the TCE removal except that almost none of the decane is removed by the aqueous phase due to the extremely low decane solubility of 0.052 mg/l.

To illustrate the effect of the NAPL residual saturation on the displacement of n-decane by steam, an additional simulation was performed in which S_{nr} was set equal to 0.25. The results of this simulation are shown in Figure 17. Unlike the previous simulations in which the NAPL formed a bank ahead of the steam front, in this case, the displacement is less than optimal, and the separate phase n-decane is found well behind the steam front. Because the saturation of liquid n-decane behind the steam front is less than S_{nr}, the liquid is immobile, and transport occurs almost entirely by evaporation and gas phase transport. The small dip in temperature in the steam zone at the upstream edge of the n-decane is due to the evaporation of the n-decane at this point. Until the time of steam breakthrough at the outlet (1.84 hours), virtually none of the n-decane is removed from the column. Following steam breakthrough, the n-decane is removed in the form of vapor with no removal as a NAPL. After 2.16 hours of steam injection, all of the n-decane has been removed from the column in vapor form. Although this process has been characterized as less than optimal, and the n-decane is not produced as a separate phase from the column, complete removal of the n-decane from the column occurs in a relatively short time.

In Figure 18, the separate phase 1-methylnapthalene saturation after the waterflood, and the temperature profile and separate phase 1-methylnapthalene saturation during the steamflood are shown for S_{nr} = 0.05. As in the high residual saturation decane simulation, during the steamflood, the 1-methylnapthalene does not form a NAPL bank ahead of the advancing steam condensation front. This lack of optimal 1-methylnapthalene mobilization is shown in Figure 19. During the steamflood, none of the 1-methylnapthalene is produced as a separate phase. At the time of steam breakthrough at the outlet (1.86 hours), only 0.26 ml of 1-methylnapthalene has been produced, all as a dissolved species in the aqueous phase. Following steam breakthrough, the 1-methylnapthalene is removed in the vapor form. Finally, 5.72 hours after the start of steam injection, all of the 1-methylnapthalene has been removed from the column. Almost all of the 1-methylnapthalene is produced as a vapor, 17.74 ml.

Since the 1-methylnapthalene was not produced as a separate phase, the steam displacement of 1-methylnapthalene under these conditions would be considered less than optimal. Although this displacement is not optimal with respect to the TCE, xylene, and low residual saturation decane steam displacement, the steam is still able to remove all of the 1-methylnapthalene in a reasonably short time. For the purpose of comparison, it would take nearly 300 hours to evaporate the 1-methylnapthalene using $25^{o}C$ air injected at a volumetric rate equal to the steam injection rate used above. This does not include the time required to de-water the medium before evaporation could take place. Removal of the 1-methylnapthalene by waterflooding would take a very long time due to the low solubility of 1-methylnapthalene (28.5

mg/l).

CONCLUSIONS

The STMVOC simulator has been successfully validated by comparisons with laboratory column steamflood experiments conducted by Hunt et al. [1988b]. With a minimum of calibration, the simulator is able to accurately reproduce the experimentally determined steam front velocity, temperature profile, pressure gradients, and rate of NAPL removal in different phases.

A simple criterion is derived which provides a necessary condition for the optimal removal of NAPLs from porous media by steam injection. It is shown that the efficiency of the steam displacement process depends on the NAPL saturated vapor pressure at the steam temperature, and on the NAPL residual saturation. The applicability of this criterion is demonstrated by the results of several numerical simulations in which different NAPLs were used. The results of this study indicate that NAPLs having boiling points less than about $175\ ^oC$ may be efficiently removed as a separate phase by steam injection.

Although the steam displacement of NAPLs with boiling points above about $175\ ^oC$ may not be as efficient as the displacement of NAPLs with lower boiling points, the rate of removal is still much larger than with air injection and vapor extraction methods.

NOTATION

A area, m^2.

C_R soil grain heat capacity, $J/kg\ K$.

C_w liquid water heat capacity, $J/kg\ K$.

$\bar{C}_g^c$ saturated chemical vapor concentration, kg/m^3.

$\bar{C}_w^c$ solubility of chemical in water, kg/m^3.

D_g^K molecular diffusivity of mass component K in a multicomponent gas, m^2/s.

E NAPL evaporation rate per unit cross sectional area, $kg/m^2 s$.

h_β specific enthalpy of phase β, J/kg.

h_{vap}^w water latent heat of vaporization, J/kg.

h_{in}^w specific enthalpy of injected water, J/kg.

K component index, K = a: air; w: water; c: chemical; h: heat.

k porous media permeability, m^2.

$k_{r\beta}$ relative permeability of the β phase.

k_{rncw} NAPL relative permeability in the presence of an irreducible water saturation.

k_{rnw} NAPL relative permeability in a two phase NAPL-water system.

k_{rng} NAPL relative permeability in a two phase NAPL-gas system.

$\dot{m}_{in}^w$ water component injection mass flux, $kg/m^2 s$.

$\dot{m}^{w}_{pro}$ water component production mass flux, kg/m^2s.

m^{w}_{in} water component injection rate, kg/s.

M^{c}_{wt} molecular weight of organic chemical K, $g/mole$.

M_n mass of NAPL per unit porous medium volume, kg/m^3.

P_β pressure in the β phase, Pa.

P_{cgw} gas-water capillary pressure, Pa.

P_{cgn} gas-NAPL capillary pressure, Pa.

P_{cnw} NAPL-water capillary pressure, Pa.

P_{wb} wellbore pressure, Pa.

P_{crit} critical pressure, Pa

P_R reference pressure, Pa.

P^{c}_{sat} saturated NAPL vapor pressure, Pa.

PI productivity index, m^3.

q_β mass rate of generation of phase β in a source element, kg/s.

q^K rate of generation of component K in a source element; for $K \neq h$: kg/s; for $K=h$: J/s.

R universal gas constant, $mJ/mole\ K$.

S_β β phase saturation.

$S_{\beta r}$ residual β phase saturation.

S_m empirical constant used in the calculation of capillary pressures.

$\bar{S}_w$ average water saturation in the steam zone.

T temperature, K.

T_o ambient temperature, K.

T_b chemical normal boiling temperature, K.

T_{crit} critical temperature, K.

T_R reference temperature, K.

T_s steam temperature, K.

V_s steam Darcy velocity, m/s.

V_{evf} residual NAPL evaporation front velocity, m/s.

V_{sf} steam condensation front velocity, m/s.

V_{crit}^K critical molar volume for mass component K, $cm^3/mole$.

X steam quality.

Z_{crit} critical compressibility.

α_{gn} constant used in the calculation of the gas-NAPL capillary pressure, $1/m$.

α_{gw} constant used in the calculation of the gas-water capillary pressure, $1/m$.

α_{nw} constant used in the calculation of the NAPL-water capillary pressure, $1/m$.

β phase index, β = g: gas phase; w: water phase; n: NAPL.

$\bar{\chi}_w^c$ chemical solubility in water (mole fraction).

η_d dipole moment, *debyes*.

λ overall porous media thermal conductivity, $W/m\ K$.

λ_D dry porous media thermal conductivity, $W/m\ K$.

λ_W water saturated porous media thermal conductivity, $W/m\ K$.

λ_n NAPL thermal conductivity, $W/m\ K$.

λ_w liquid water thermal conductivity, $W/m\ K$.

μ_β β phase viscosity, kg/ms.

μ_{nR} reference NAPL viscosity, kg/ms.

ρ_β density of the β phase, kg/m^3.

ρ_s steam density, kg/m^3.

ρ_{nsR} reference NAPL density, kg/m^3.

ρ_R soil grain density, kg/m^3.

ϕ porosity.

ω Pitzer's acentric factor.

ω_β^K mass fraction of mass component K in the β phase.

ACKNOWLEDGEMENTS

This work was supported in part by the Director, Office of Energy Research, Office of Basic Energy Sciences, Engineering and Geosciences Division of the U.S. Department of Energy, and in part pursuant to Interagency Agreement DW89931336-01-07 between the U.S. Environmental Protection Agency and the U.S. Department of Energy under contract DE-AC03-76SF00098. The authors would like to thank C. H. Lai, H. W. Dorgarten, and C. F. Tsang for reviewing this

manuscript.

REFERENCES

API Division of Refining, Technical Data Book, Petroleum Refining, American Petroleum Institute, Refining Department, Washington, 1977.

Aziz, K. and A. Settari, Petroleum Reservoir Simulation, Applied Science Publishers, London, 1979.

Devitt, D. A., R. B. Evans, W. A. Jury, T. H. Starks, B. Eklund, A. Sholsan, and J. J. van Ee, Soil Gas Sensing for Detection and Mapping of Volatile Organics, U. S. Environmental Protection Agency, Las Vegas, Nev., 1987.

Falta, R. W., K. Pruess, I. Javandel, and P. A. Witherspoon, Numerical modeling of steam injection for the removal of nonaqueous phase liquids from the subsurface, 1. Numerical formulation, Water Resources Research, this issue.

Frick, T. (Ed.), Petroleum Production Handbook, 2nd ed., Society of Petroleum Engineers of AIME, Dallas, TX, 1962.

Hunt, J. R., N. Sitar, and K. S. Udell, Nonaqueous phase liquid transport and cleanup, 1. Analysis of mechanisms, Water Resources Research, 24(8), 1247-1258, 1988a.

Hunt, J. R., N. Sitar, and K. S. Udell, Nonaqueous phase liquid transport and cleanup, 2. Experimental studies, Water Resources Research, 24(8), 1259-1269, 1988b.

Menegus, D. K., and K. S. Udell, A study of steam injection into water saturated capillary porous media, in Heat Transfer in Porous Media and Particulate Flows, vol. 46, 151-157, American Society of Mechanical Engineers, New York, 1985.

Parker, J. C., R. J. Lenhard, and T. Kuppusamy, A parametric model for constitutive properties governing multiphase flow in porous media, Water Resources Research, 23(4), 618-624, 1987.

Pruess, K., C. Calore, R. Celati, and Y. S. Wu, An analytical solution for heat transfer at a boiling front moving through a porous medium, Int. J. Heat Mass Transfer, 30(12), 2595-2602, 1987.

Reid, R. C., J. M. Prausnitz, and B. E. Poling, The Properties of Gases and Liquids, McGraw-Hill, New York, 1987.

Stewart, L. D., and K. S. Udell, Mechanisms of residual oil displacement by steam injection, SPE Reservoir Engineering, 1233-1242, November, 1988.

Stone, H. L., Probability model for estimating three-phase relative permeability, Journal of Petroleum Technology, 22(1), 214-218, 1970.

Udell, K. S. and L. D. Stewart, Field study of in situ steam injection and vacuum extraction for recovery of volatile organic solvents, University of California, UCB-SEEHRL Report No. 89-2, 1989.

van Genuchten, M. T., A closed-form equation for predicting the hydraulic conductivity of unsaturated soils, Soil Sci. Soc. Am. J., 44, 892-898, 1980.

Table 1. Data Used in the Simulation of the Baseline Steam Injection Experiment of Hunt *et al.* [1988b]

Parameter	Value
Permeability	$k = 1.6 \times 10^{-11}$ m^2
Porosity	$\phi = 0.385$
Soil grain heat capacity	$C_R = 1000$ kJ/kg°C
Soil grain density	$\rho_R = 2650$ kg/m^3
Dry media thermal conductivity	$\lambda_D = 2.86$ W/m°C
Water saturated media thermal conductivity	$\lambda_W = 3.10$ W/m°C
Initial temperature	T = 22°C
Water component injection rate	$m_{in}^w = 3.534 \times 10^{-5}$ kg/s
Specific enthalpy of injected water	
$t \leq 468$ s	$h_{in}^w = 419$ kJ/kg
$t > 468$ s	$h_{in}^w = 1{,}562$ kJ/kg
Outlet pressure	$P_{wb} = 101{,}400$ Pa
Productivity index	PI = 3.59×10^{-12} m^3

Table 2. Relative Permeability and Capillary Pressure Curves Used in the Baseline Steam Injection Simulation

Parameter	Value
Gas phase relative permeability	$k_{rg} = \left[S_g\right]^n$
Aqueous phase relative permeability ($S_w > S_{wr}$)	$k_{rw} = \left[\frac{S_w - S_{wr}}{1 - S_{wr}}\right]^n$
	$S_{wr} = 0.15$; $n = 3$
Gas–water capillary pressure	$P_{cgw} = \frac{\rho_w g}{\alpha_{gw}} \left[\left[\frac{S_w - S_m}{1 - S_m}\right]^{-1/m} - 1\right]^{1/n}$
	$m = 1 - 1/n$; $n = 1.84$; $\alpha_{gw} = 5.24/m$; $S_m = 0$

Table 3. Constants Used to Calculate the Thermophysical Properties of Trichloroethylene

Constant	Value	Comment
Molecular weight*	$M^c_{wt} = 131.4$ g/mole	
Critical temperature*	$T_{crit} = 572.0$ K	
Critical pressure*	$P_{crit} = 50.5$ bar	
Critical compressibility*	$Z_{crit} = 0.265$	
Critical volume*	$V^c_{crit} = 256.0$ cm^3/mole	
Normal boiling point*	$T_b = 360.4$ K	$T_b = 87.3$°C
Pitzer's acentric factor**	$\omega = 0.213$	
Dipole moment*	$\eta_d = 0.9$ debyes	
Aqueous solubility†	$\bar{\chi}^c_w = 1.5095 \times 10^{-4}$	$\bar{C}^c_w = 1,100$ mg/l
Vapor pressure constants*	a = −7.38190 b = 1.94817 c = −3.03294 d = −5.34536	
Ideal gas heat capacity constants*	a = 30.17 b = 0.2287 c = -2.229×10^{-4} d = 8.244×10^{-8}	
Reference liquid density*	$\rho_{nsR} = 1462.0$ kg/m^3 at $T_R = 293.0$ K	
Reference liquid viscosity‡	$\mu_{nR} = 0.59$ cP at $T_R = 293.0$ K	

*Reid *et al.* [1987]
†Devitt *et al.* [1987]
‡Hunt *et al.* [1988a]

Table 4. Relative Permeability and Capillary Pressure Curves Used in the TCE Displacement Simulation

Parameter	Value
Gas phase relative permeability	$k_{rg} = (S_g)^n$
Aqueous phase relative permeability ($S_w > S_{wr}$)	$k_{rw} = \left[\frac{S_w - S_{wr}}{1 - S_{wr}}\right]^n$
NAPL relative permeability in a gas–NAPL system	$k_{rng} = (1 - S_g - S_{wr})^n$
NAPL relative permeability in a water–NAPL system	$k_{rnw} = (1 - S_w)^n$
NAPL relative permeability ($S_n > S_{nr}$)	$k_{rn} = \frac{(S_n - S_{nr})\, k_{rnw}\, k_{rng}}{S^* k_{rncw} \left[1 - \frac{(S_w - S_{wr})}{S^*}\right] \left[1 - \frac{S_g}{S^*}\right]}$
	$S^* = (1 - S_{wr} - S_{nr})$; $k_{rncw} = (1 - S_{wr})^n$; $n = 3$; $S_{wr} = 0.15$; $S_{nr} = 0.05$
Gas–NAPL capillary pressure	$P_{cgn} = \frac{\rho_w g}{\alpha_{gn}} \left[\left[\frac{S_w + S_n - S_m}{1 - S_m}\right]^{-1/m} - 1\right]^{1/n}$
Gas–water capillary pressure	$P_{cgw} = P_{cgn} + \frac{\rho_w g}{\alpha_{nw}} \left[\left[\frac{S_w - S_m}{1 - S_m}\right]^{-1/m} - 1\right]^{1/n}$
	$m = 1 - 1/n$; $n = 1.84$; $\alpha_{gn} = 10.0/m$; $\alpha_{nw} = 11.0/m$; $S_m = 0$

Table 5. Comparison of Residual Saturation Evaporation Velocities for Several Organic Liquids

Chemical	Boiling Point[a] T_b, °C	Saturated Vapor Concentration at 100°C, C_g^c, kg/m^3	Evaporation Front Velocity V_{ef}, m/day	V_{ef}/V_{sf}
o-xylene, S_{nr} = .05	144.5	0.904	72.2	5.6
n-decane, S_{nr} = .05	174.2	0.440	42.7	3.3
S_{nr} = .25			8.5	0.7
1-methylnapthalene, S_{nr} = .05	244.8	0.043	2.9	0.2

[a] Reid *et al.* [1987]

Table 6. Constants Used to Calculate the Thermophysical Properties of Several Organic Liquids

Constant	Value		
	o-xylene	n-decane	1-methylnapthalene
Molecular weight*	M^c_{wt} = 106.2 g/mole	M^c_{wt} = 142.3 g/mole	M^c_{wt} = 142.2 g/mole
Critical temperature*	T_{crit} = 630.3 K	T_{crit} = 617.7 K	T_{crit} = 772.0 K
Critical pressure*	P_{crit} = 37.3 bar	P_{crit} = 21.2 bar	P_{crit} = 36.0 bar
Critical compressibility*	Z_{crit} = 0.262	Z_{crit} = 0.249	Z_{crit} = 0.234
Critical volume*	V^c_{crit} = 369 cm^3/mole	V^c_{crit} = 603 cm^3/mole	V^c_{crit} = 462 cm^3/mole
Normal boiling point*	T_b = 417.6 K (144.5°C)	T_b = 447.3 K (174.2°C)	T_b = 517.9 K (244.8°C)
Pitzer's acentric factor*	ω = 0.310	ω = 0.489	ω = 0.310
Dipole moment*	η_d = 0.5 debyes	η_d = 0.0 debyes	η_d = 0.5 debyes
Aqueous solubility†	$\bar{\chi}^c_w = 2.975 \times 10^{-5}$ (175 mg/l)	$\bar{\chi}^c_w = 6.5966 \times 10^{-8}$ (0.052 mg/l)	$\bar{\chi}^c_w = 3.6176 \times 10^{-6}$ (28.5 mg/l)
Vapor pressure constants*	a = −7.53357 b = 1.40968 c = −3.10985 d = −2.85992	a = −8.56523 b = 1.97756 c = −5.81971 d = −0.29982	a = −7.56390 b = 1.19577 c = −3.38134 d = −2.86388
Ideal gas heat capacity constants*	a = 15.85 b = 0.5962 c = -3.443×10^{-4} d = 7.528×10^{-8}	a = −7.193 b = 0.9609 c = -5.288×10^{-4} d = 1.131×10^{-7}	a = −64.82 b = 0.9387 c = -6.942×10^{-4} d = 2.016×10^{-7}
Reference liquid density*	ρ_{nsR} = 880.0 kg/m^3 at T_R = 293.0 K	ρ_{nsR} = 730.0 kg/m^3 at T_R = 293.0 K	ρ_{nsR} = 1020 kg/m^3 at T_R = 293.0 K
Liquid viscosity constants*	a = −3.332 b = 1.039×10^3 c = -1.768×10^{-3} d = 1.076×10^{-6}	a = −4.460 b = 1.286×10^3 c = 0 d = 0	a = — b = — c = — d = —
or Reference liquid viscosity‡	μ_{nR} = — at T_R = —	μ_{nR} = — at T_R = —	μ_{nR} = 1.1 cP at T_R = 355.4 K

*Reid *et al.* [1987]
†Devitt *et al.* [1987]
‡API [1977]

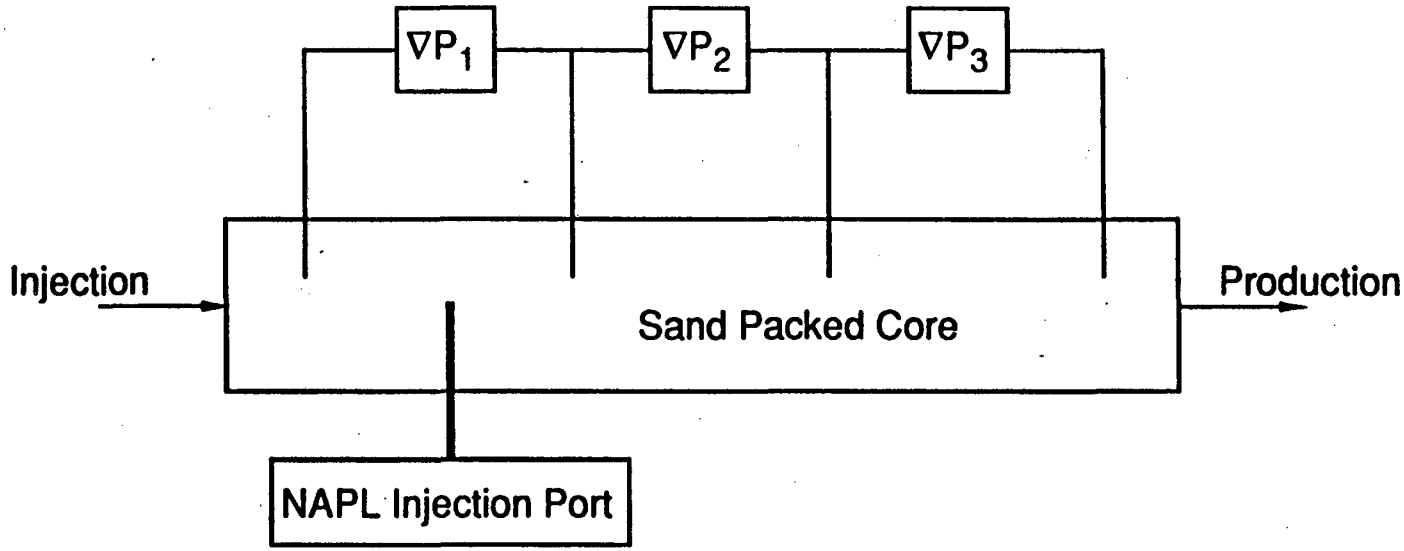

Figure 1. Experimental geometry used by Hunt et al. [1988b].

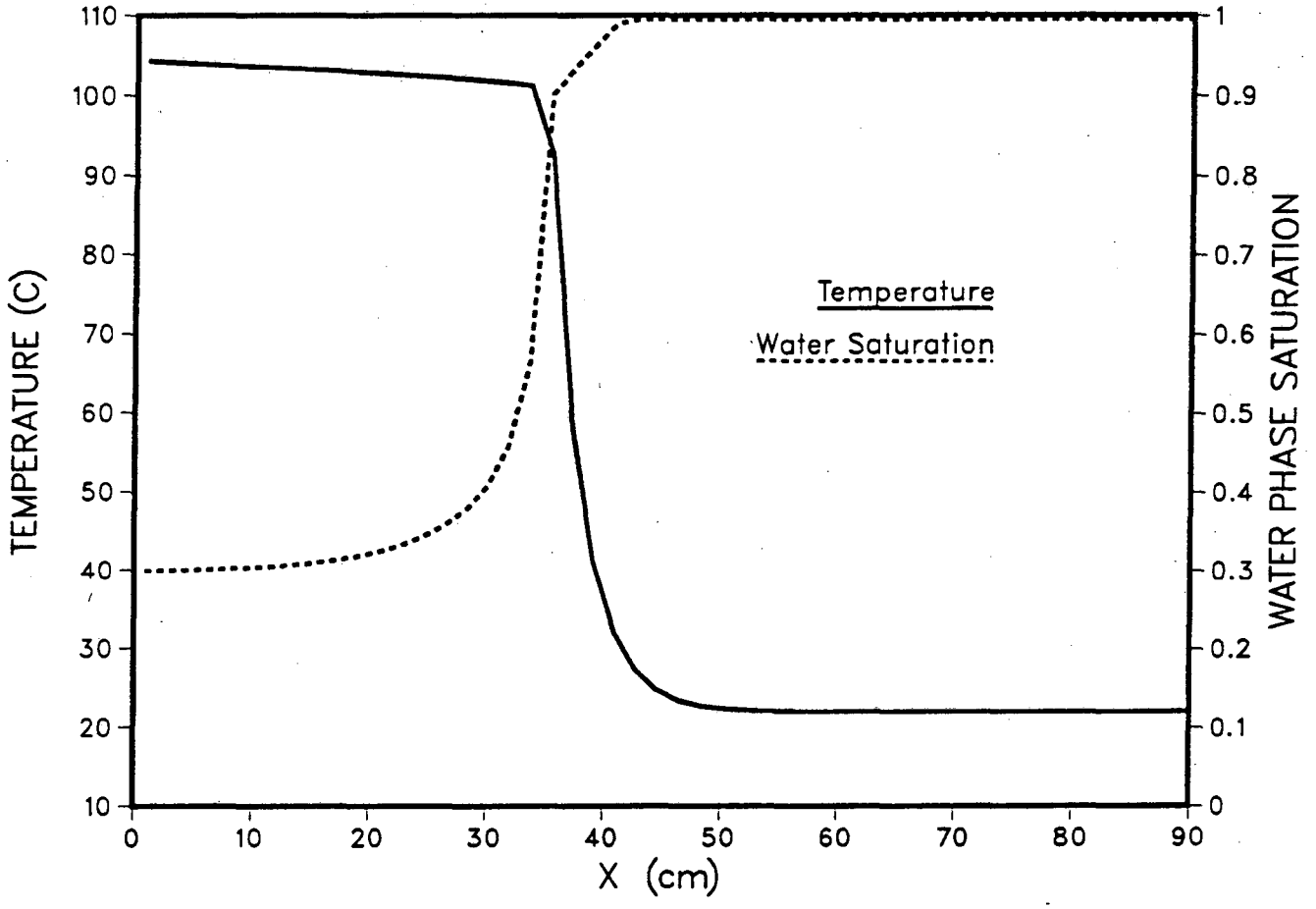

Figure 2. Calculated temperature and water saturation distribution 3000 s after the start of steam injection.

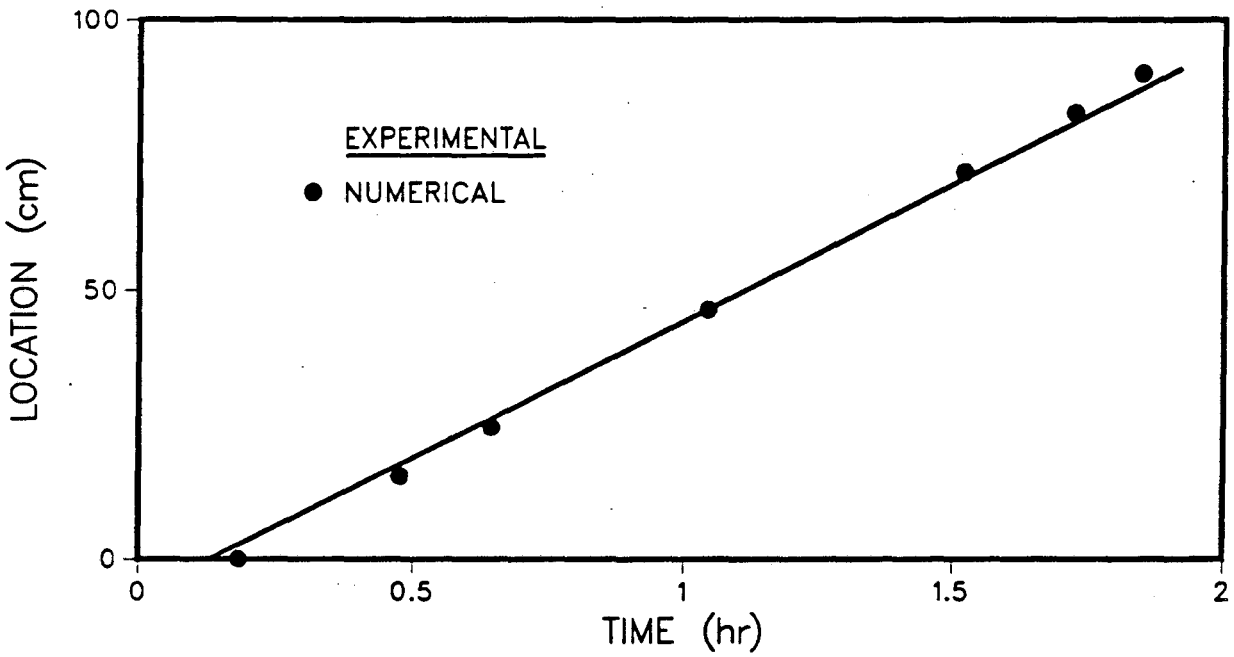

Figure 3. Comparison of calculated steam condensation front location with the experimental data of Hunt et al. [1988b] for the baseline experiment.

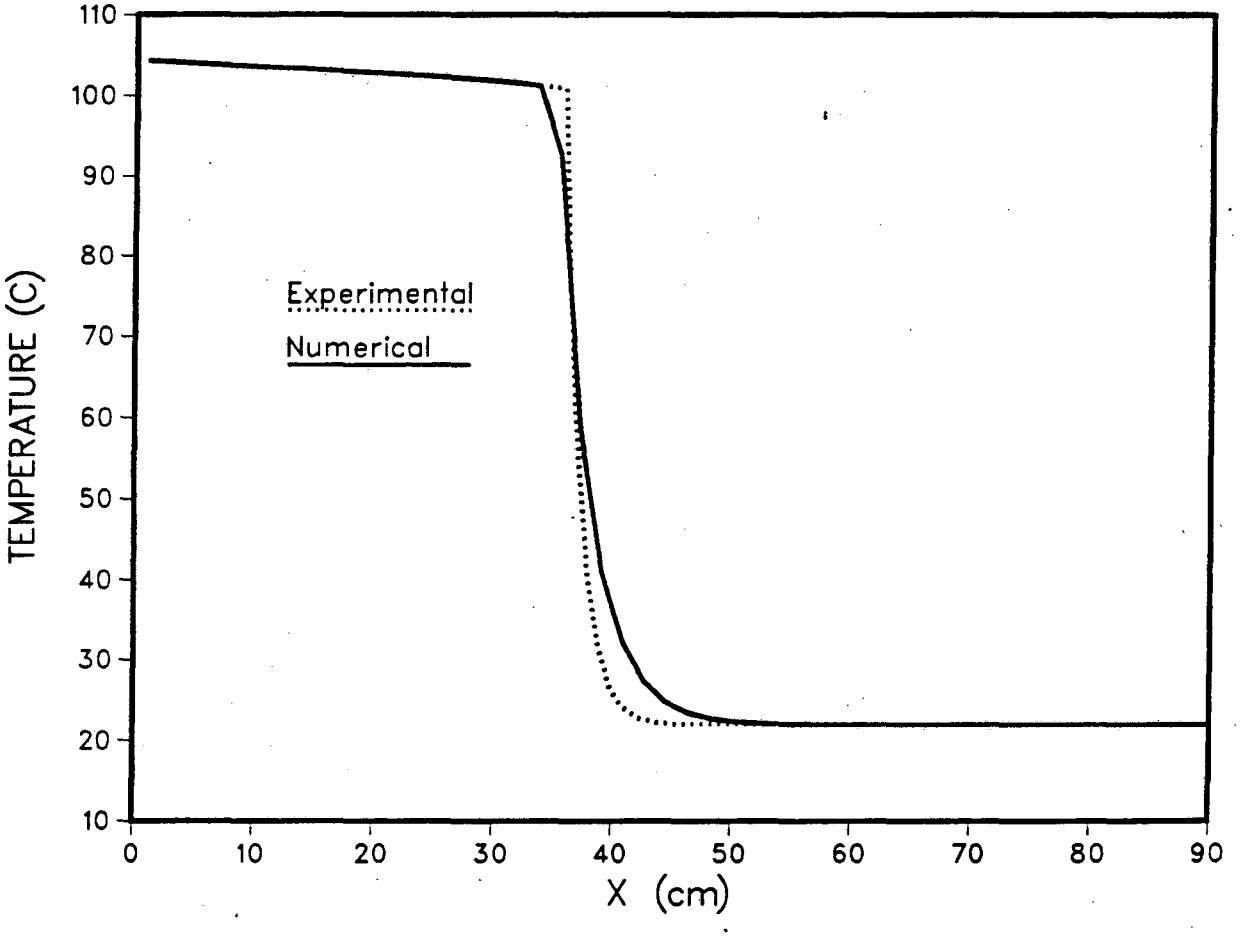

Figure 4. Comparison of calculated temperature profile with the experimental data of Hunt et al. [1988b] for the baseline experiment.

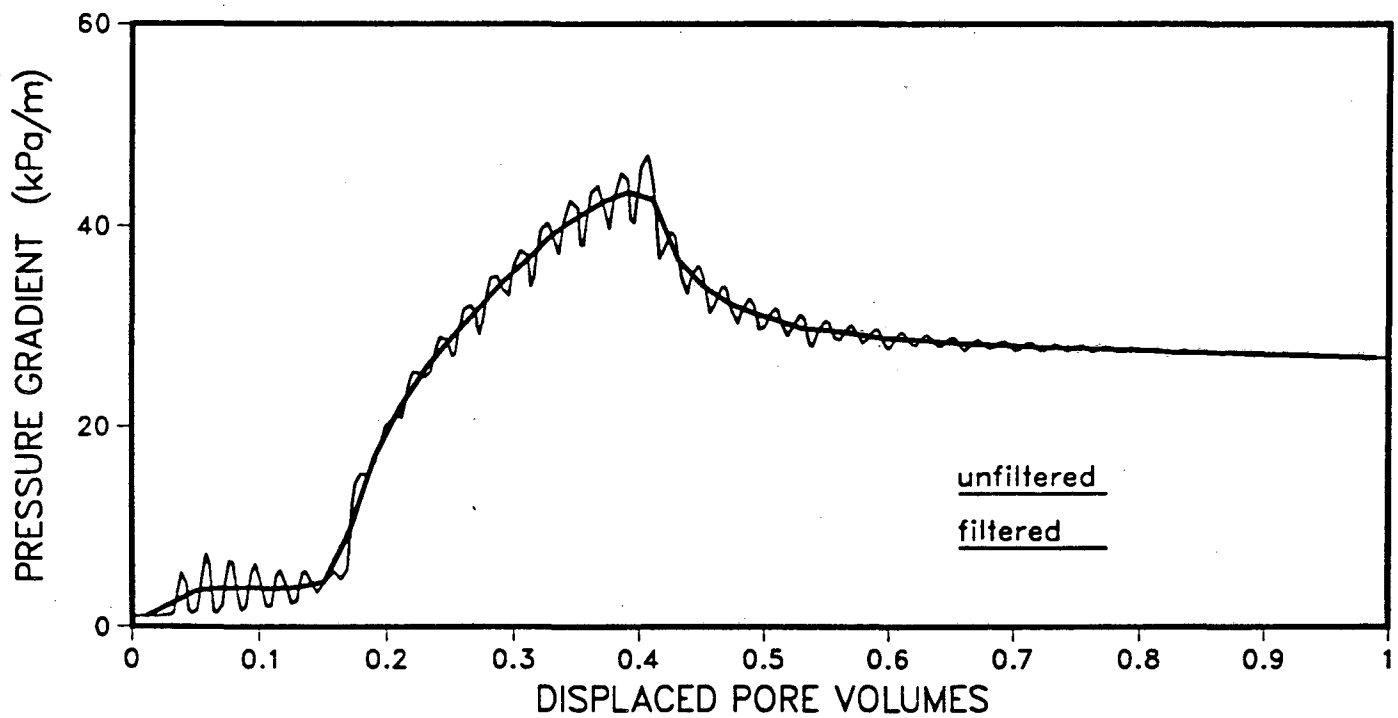

Figure 5. Calculated pressure gradient.

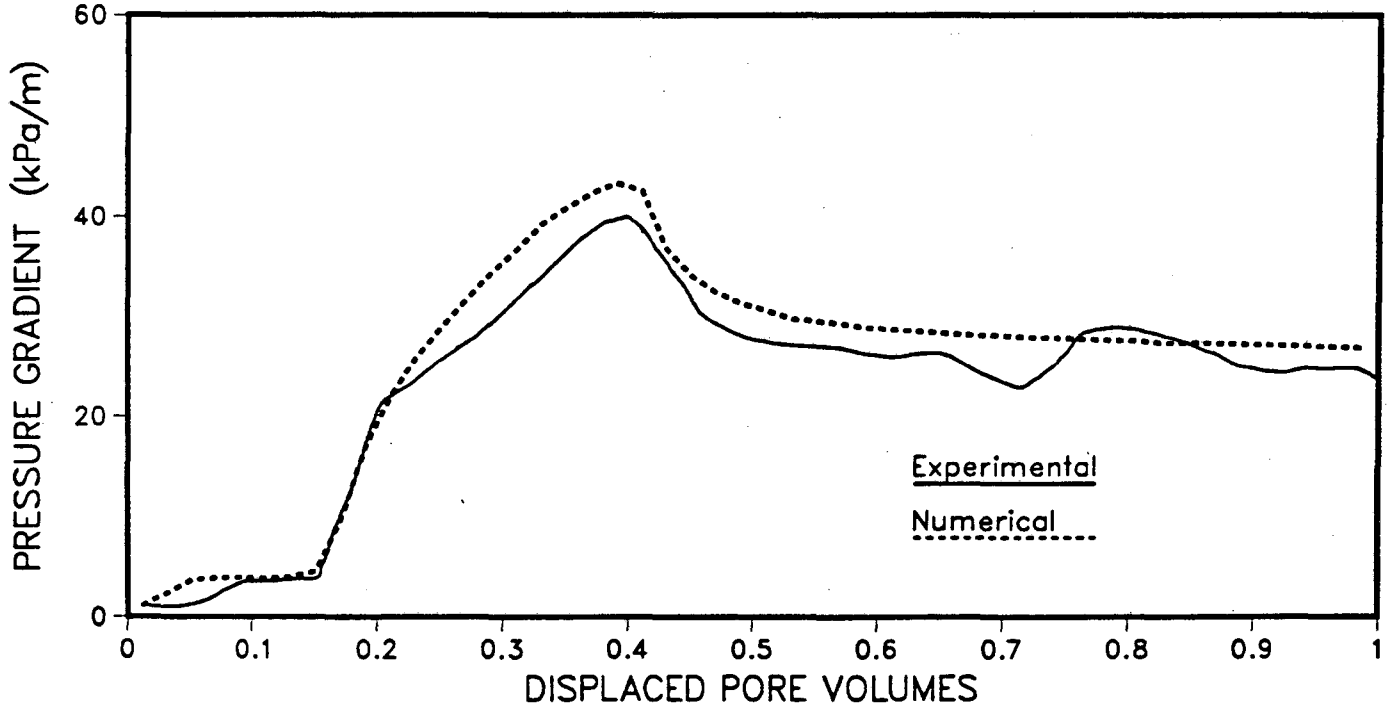

Figure 6. Comparison of calculated pressure gradient with the experimental data of Hunt et al. [1988b] for the baseline experiment.

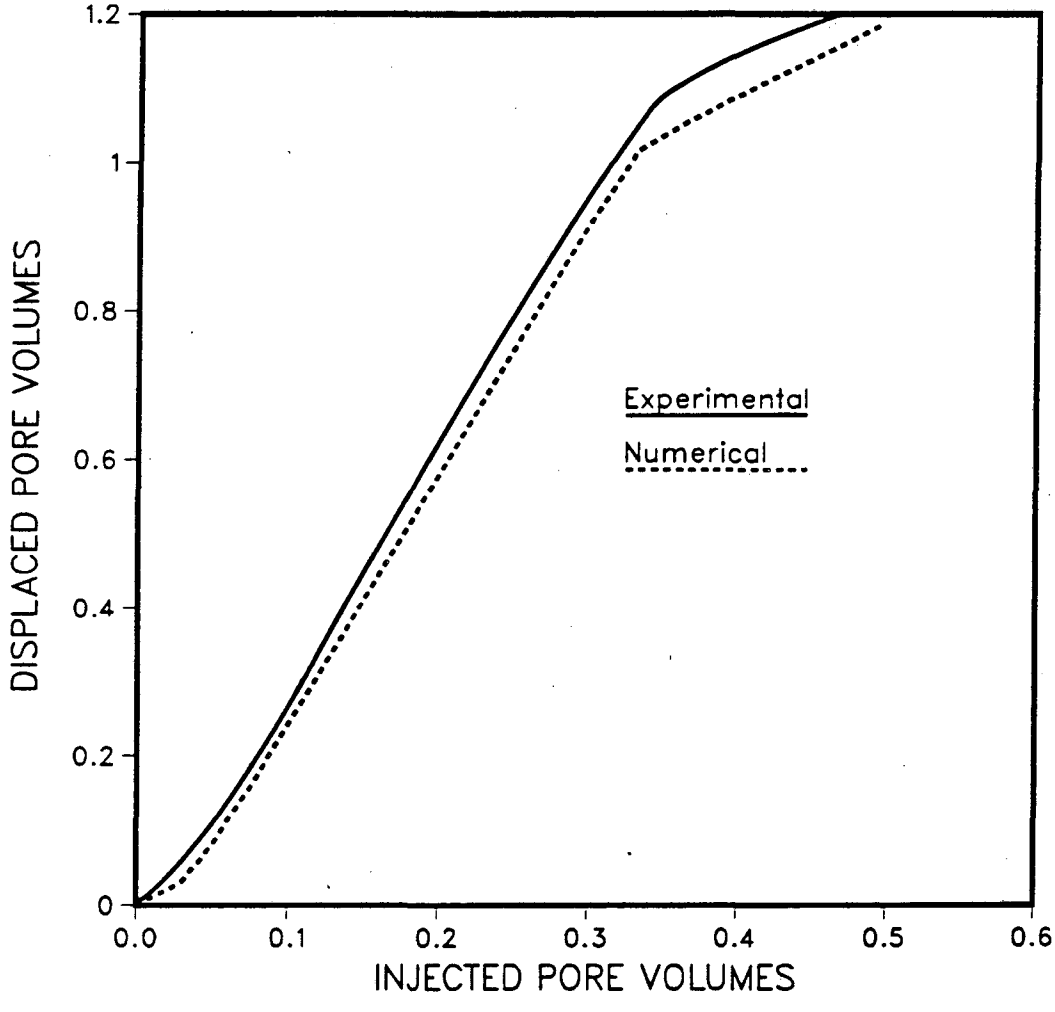

Figure 7. Comparison of calculated value of produced liquid volume with the experimental data of Hunt et al. [1988b] for the baseline experiment.

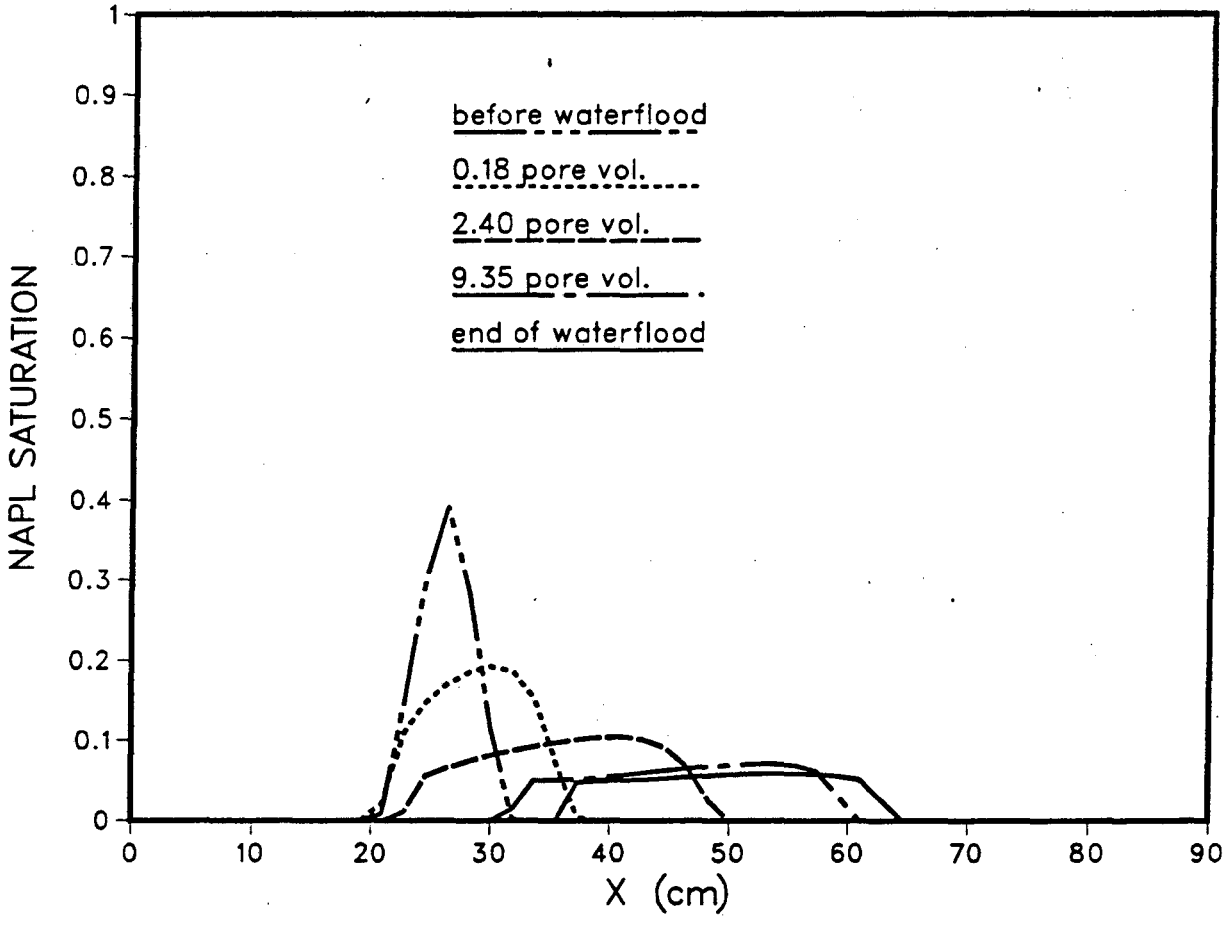

Figure 8. Calculated separate phase TCE distribution during waterflood.

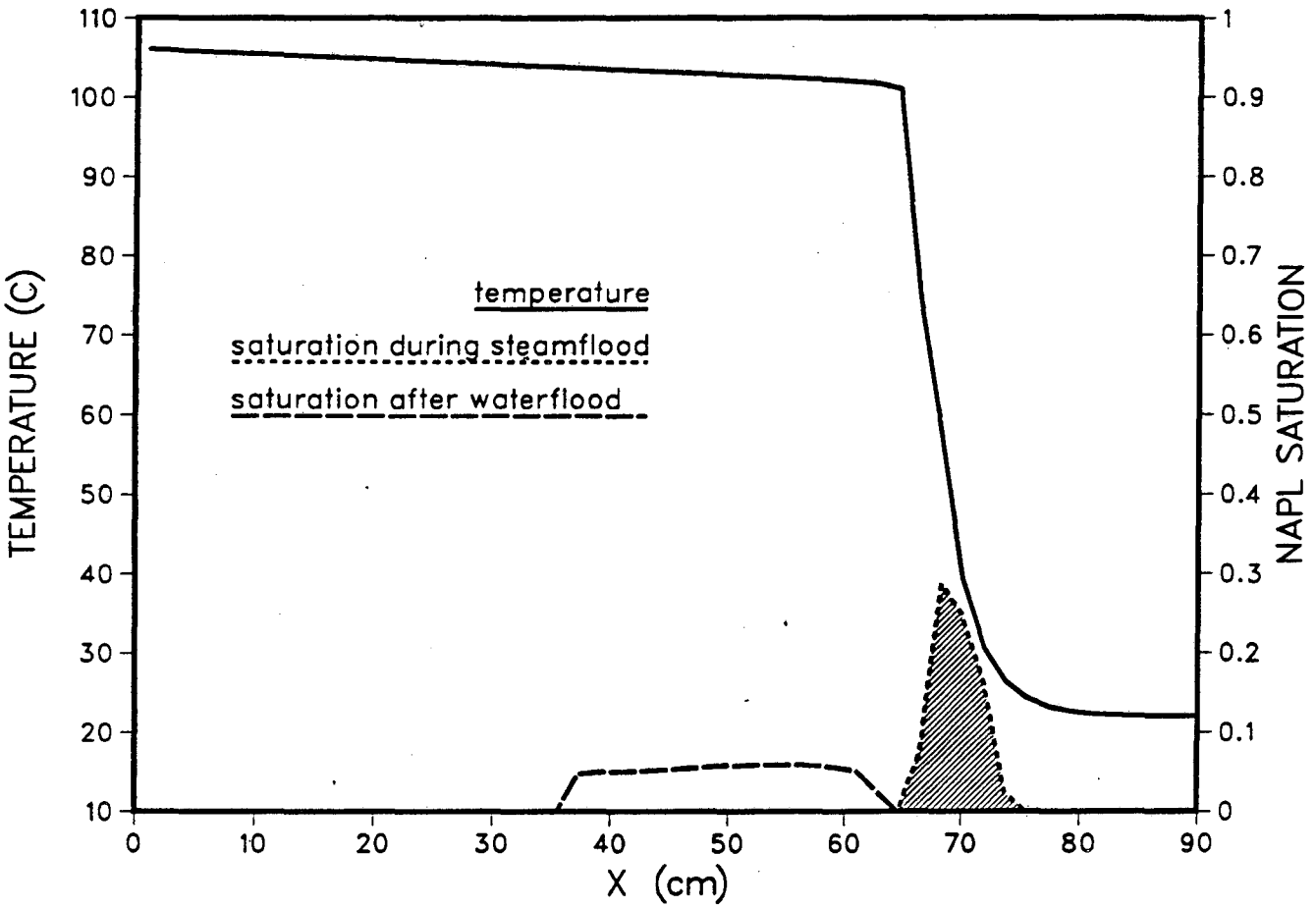

Figure 9. Calculated separate phase TCE distribution after waterflood, and temperature profile and separate phase TCE distribution 5000 s after the start of steam injection.

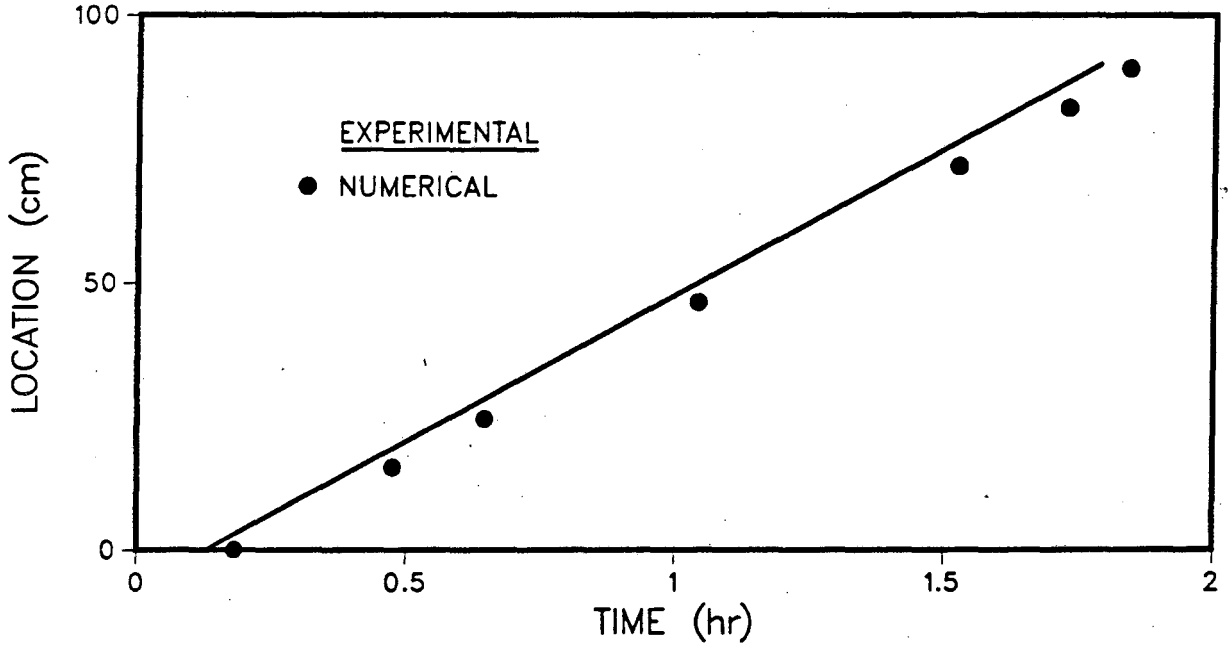

Figure 10. Comparison of calculated steam condensation front location with the experimental data of Hunt et al. [1988b] for the TCE displacement experiment.

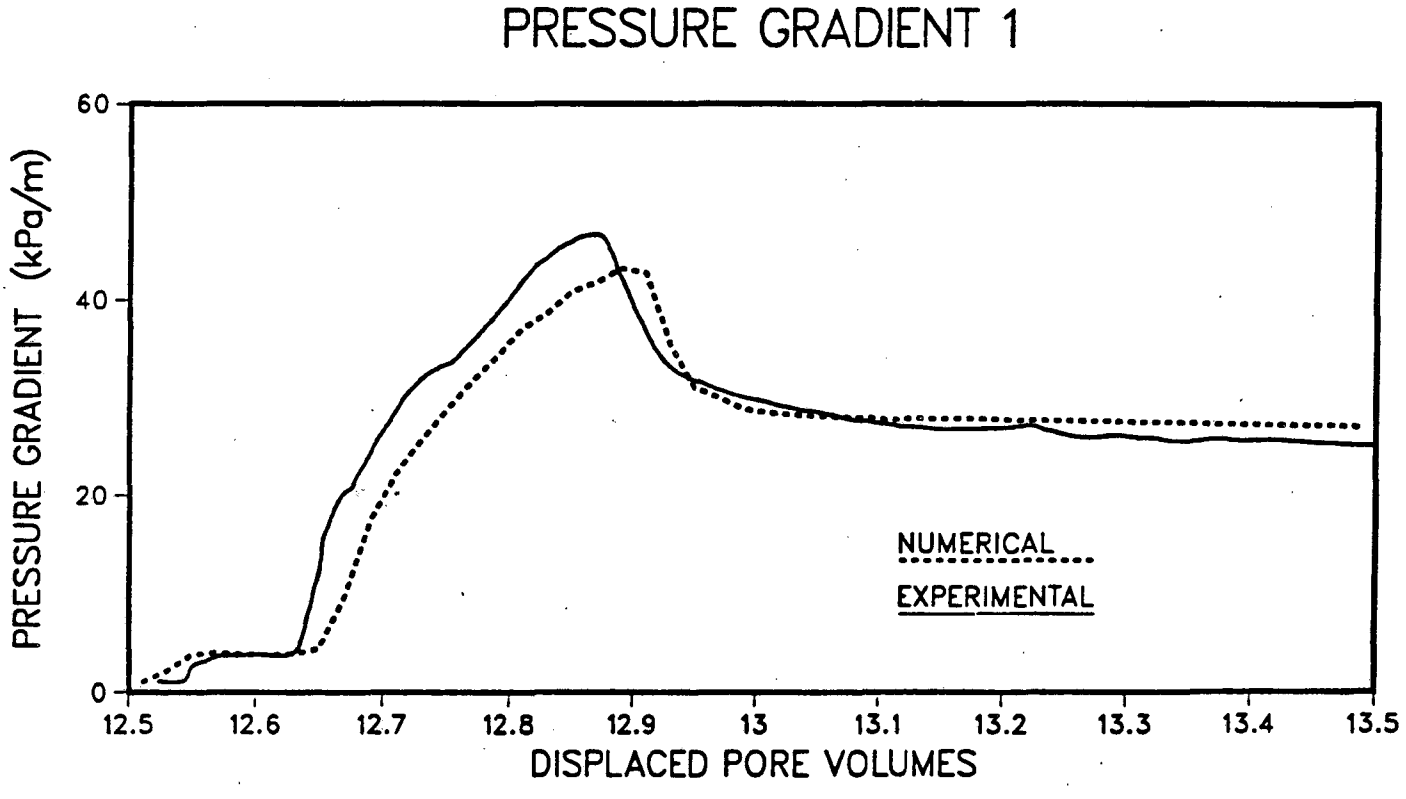

Figure 11. Comparison of calculated pressure gradient with the experimental data of Hunt et al. [1988b] for the TCE displacement experiment.

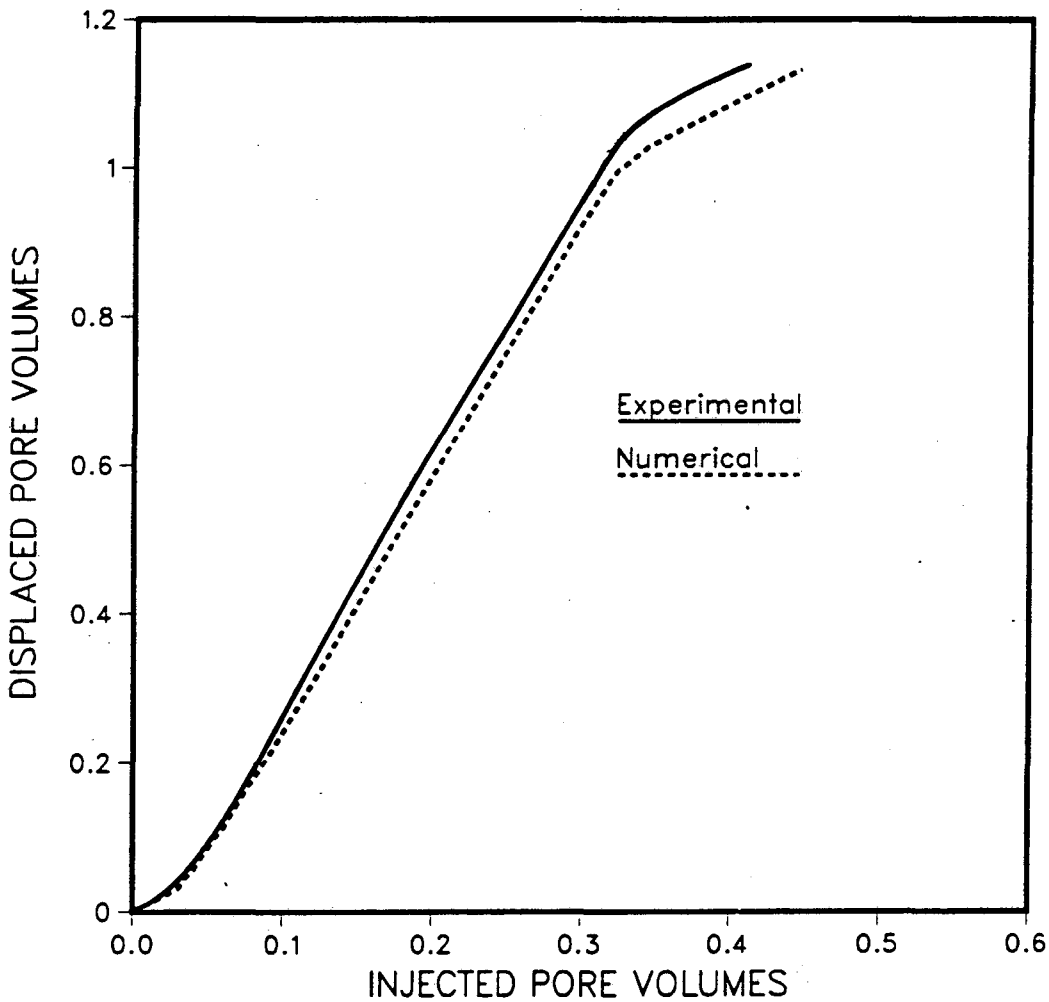

Figure 12. Comparison of calculated value of produced liquid volume with the experimental data of Hunt et al. [1988b] for the TCE displacement experiment.

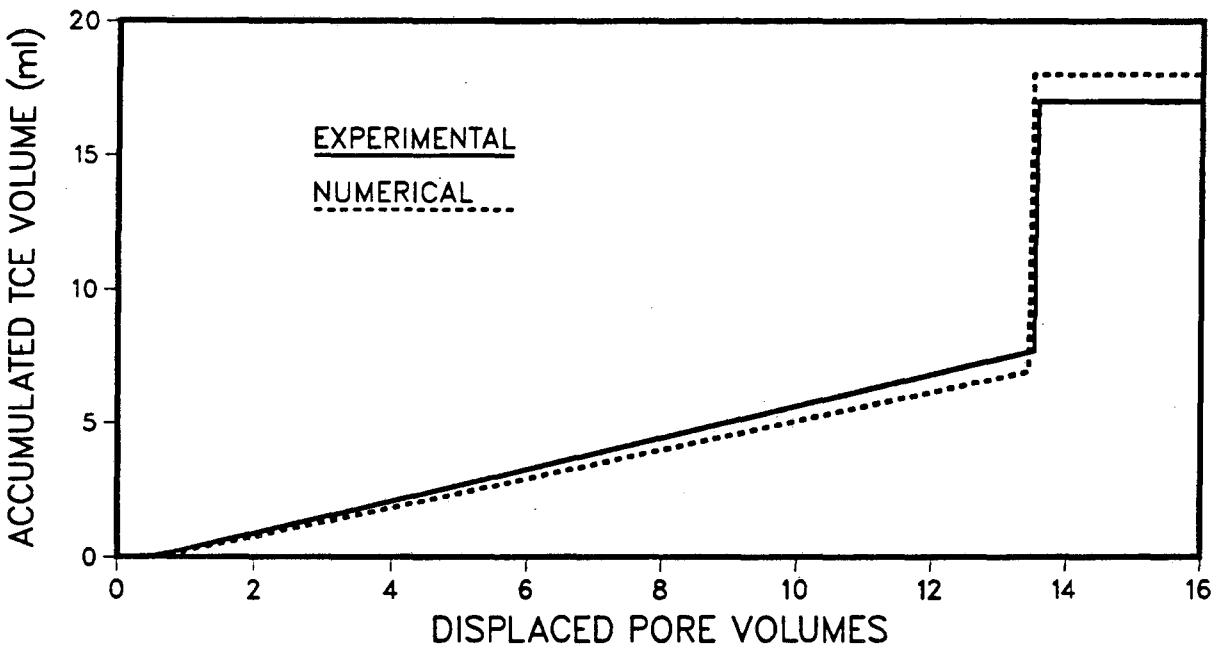

Figure 13. Comparison of calculated cumulative volume of TCE removed with the experimental data of Hunt et al. [1988b].

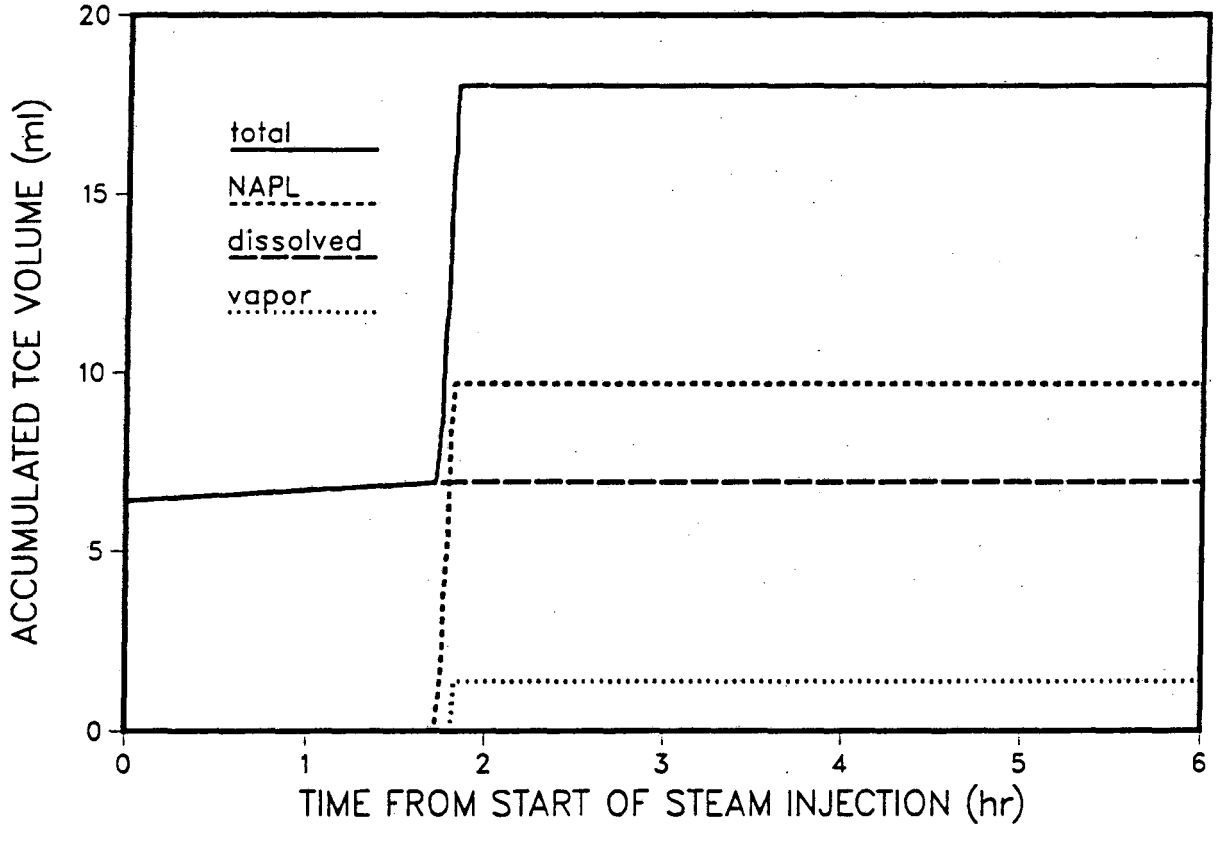

Figure 14. Volume of TCE removed in each phase during simulation.

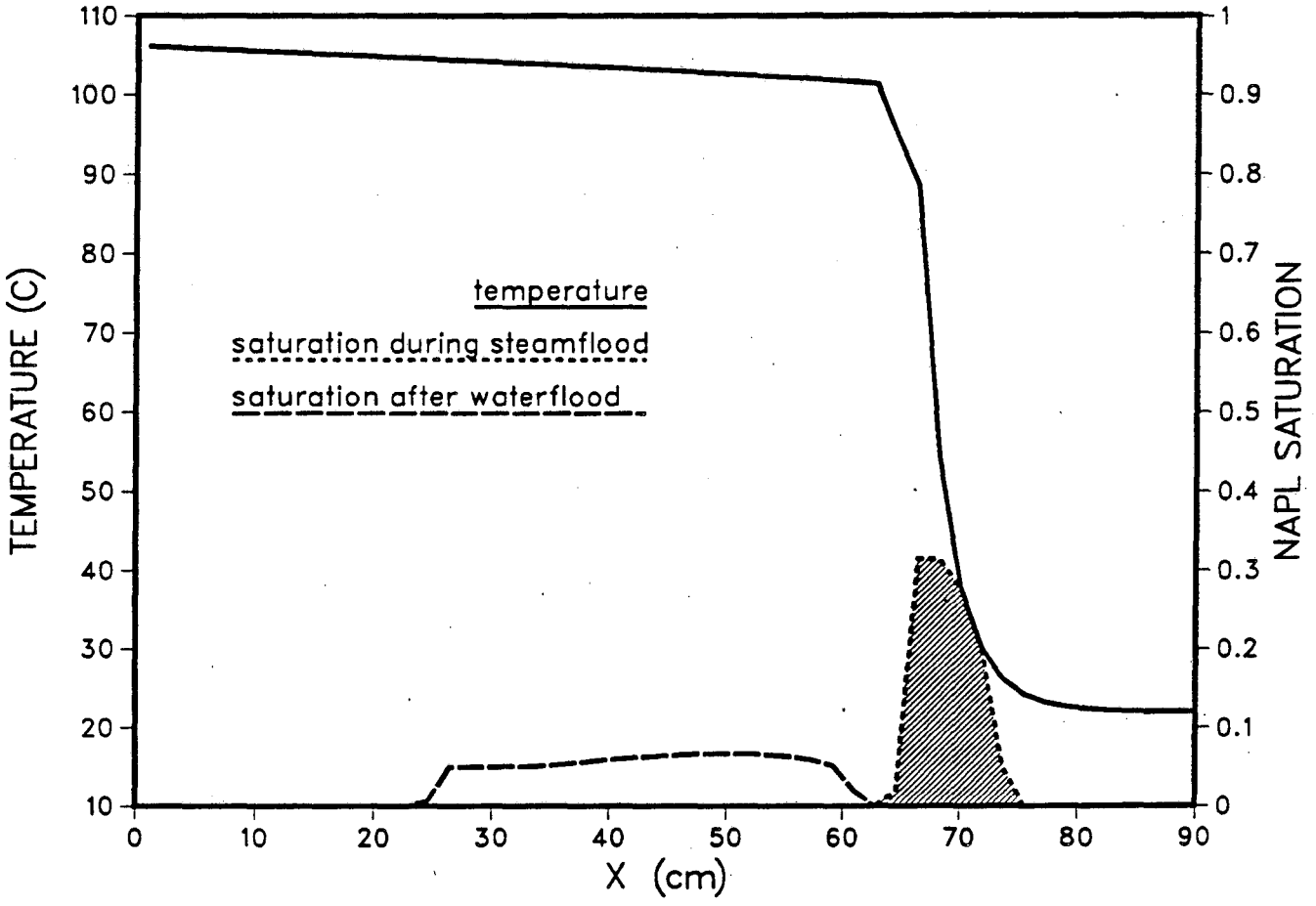

Figure 15. Calculated separate phase o-xylene saturation after waterflood, and temperature profile and separate phase o-xylene saturation after 5000 s of steam injection. S_{nr} = 0.05.

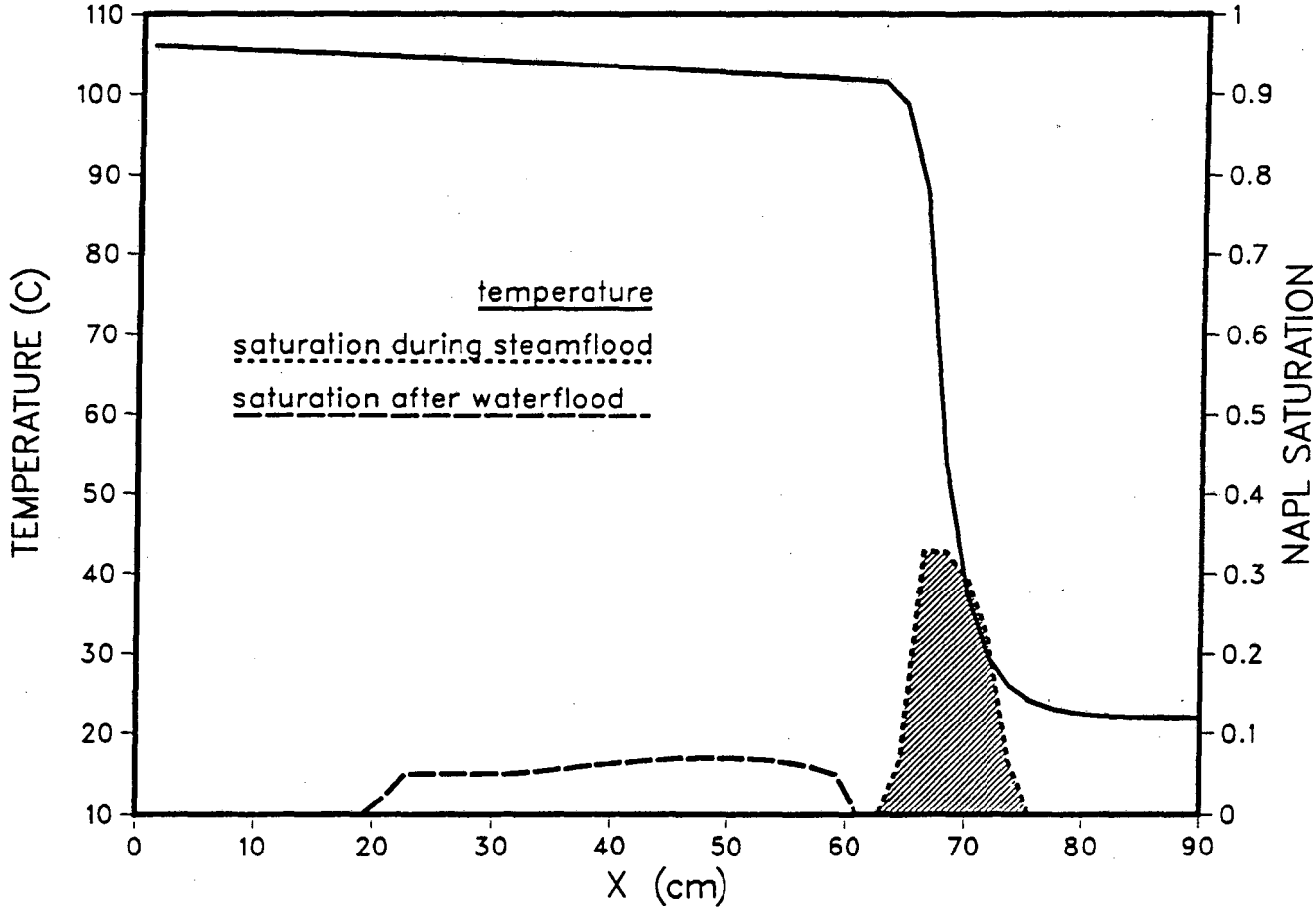

Figure 16. Calculated separate phase n-decane saturation after waterflood, and temperature profile and separate phase n-decane saturation after 5000 s of steam injection. S_{nr} = 0.05.

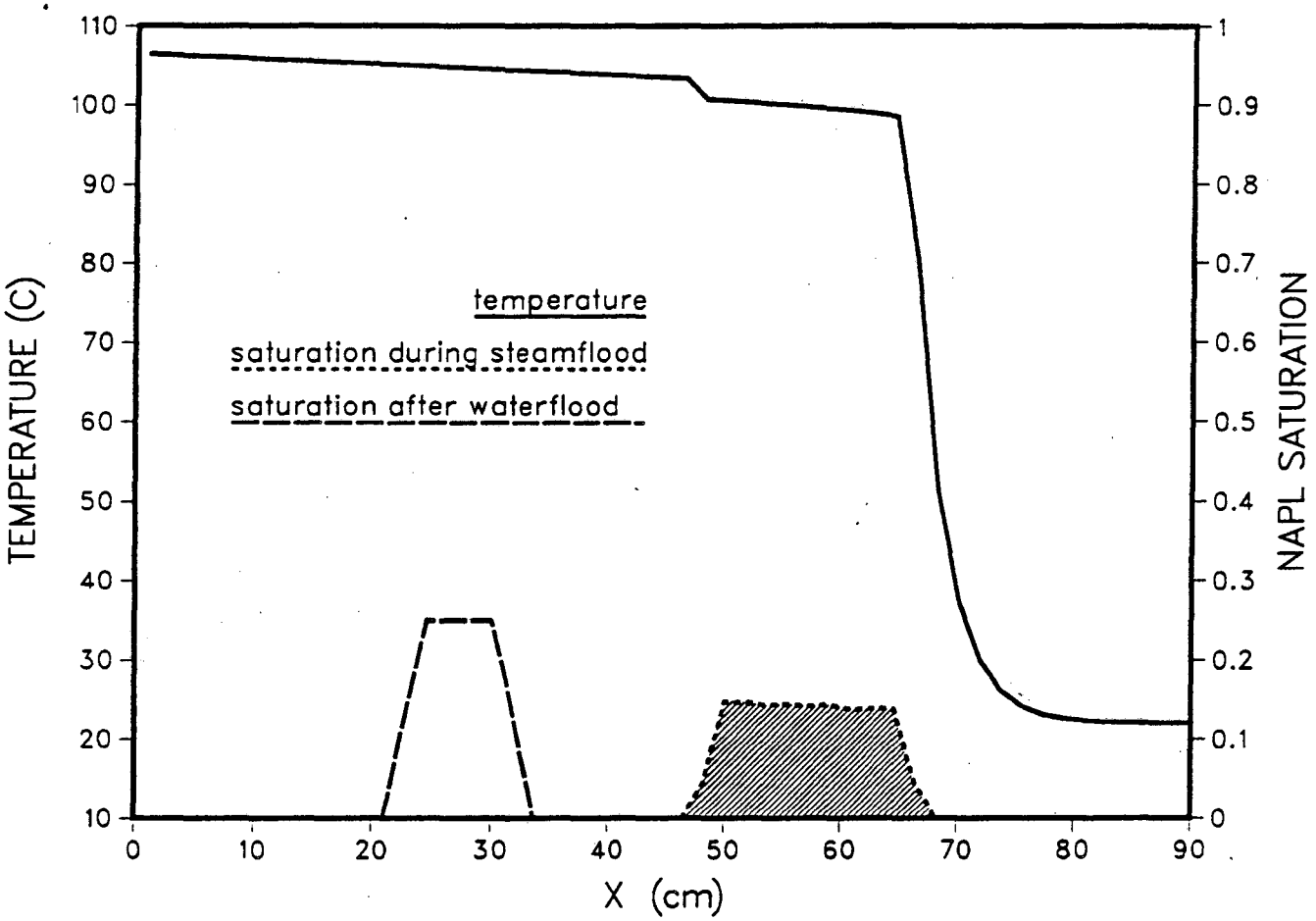

Figure 17. Calculated separate phase n-decane saturation after waterflood, and temperature profile and separate phase n-decane saturation after 5000 s of steam injection. S_{nr} = 0.25.

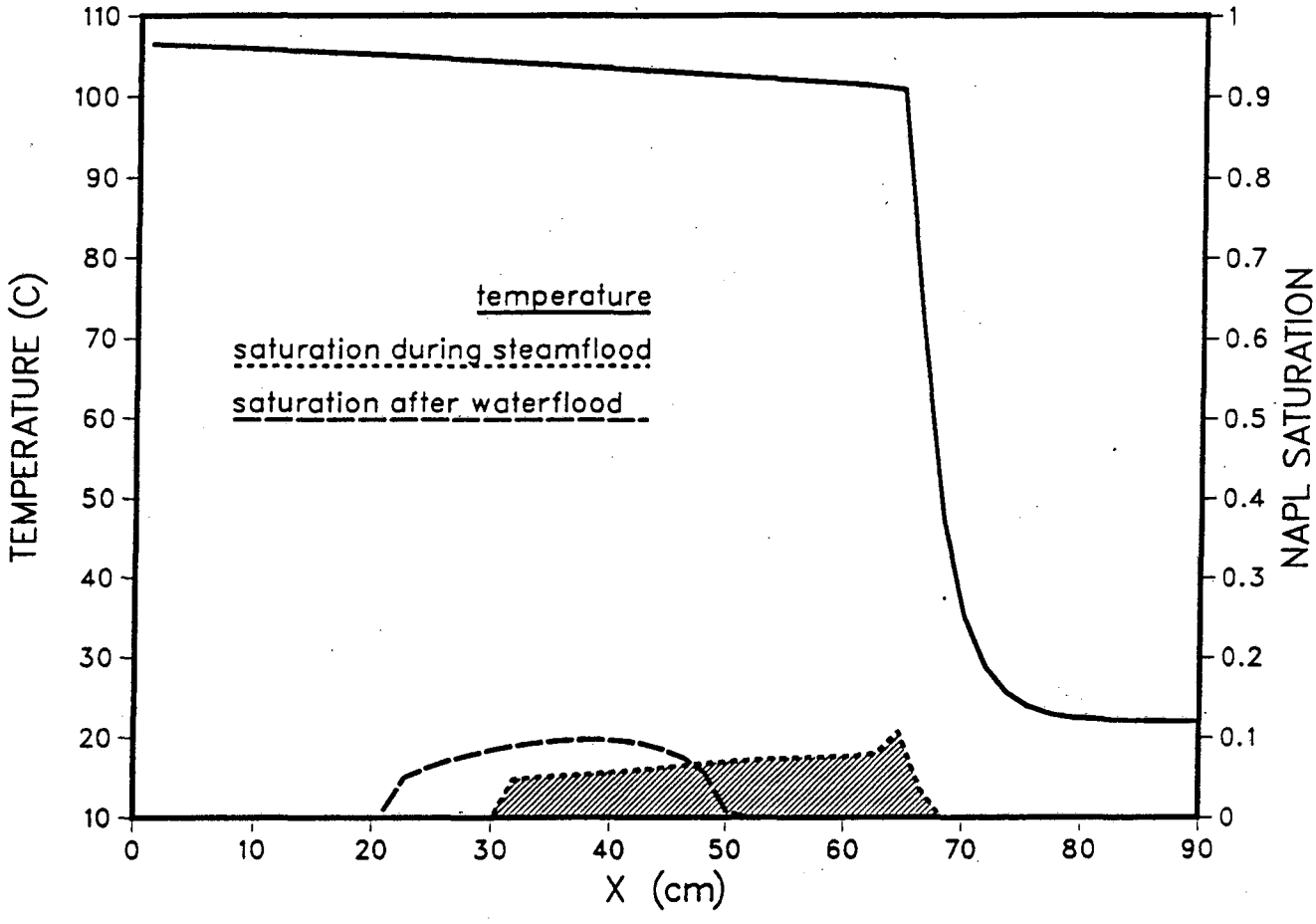

Figure 18. Calculated separate phase 1-methylnapthalene saturation after waterflood, and temperature profile and separate phase 1-methylnapthalene saturation after 5000 s of steam injection. S_{nr} = 0.05.

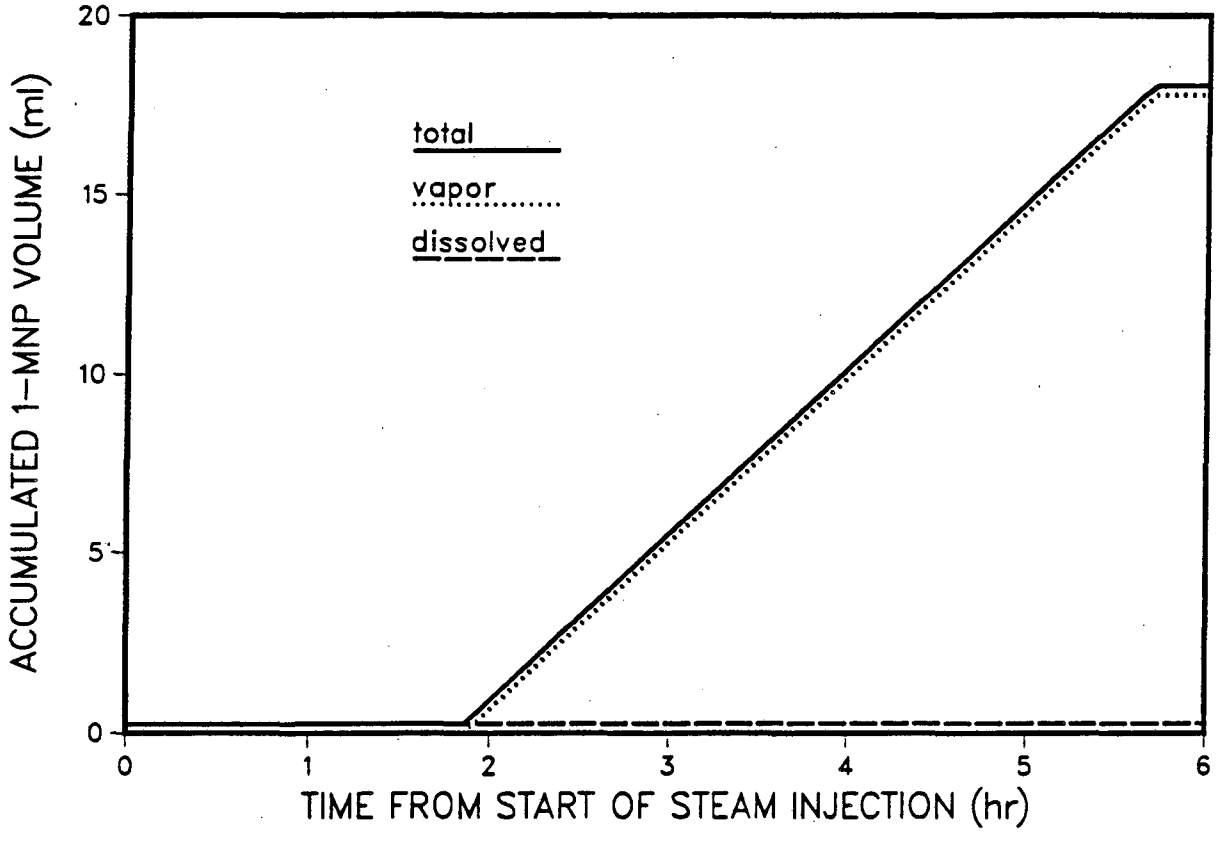

Figure 19. Volume of 1-methylnapthalene removed in each phase during simulation, $S_{nr} = 0.05$.

LAWRENCE BERKELEY LABORATORY
UNIVERSITY OF CALIFORNIA
INFORMATION RESOURCES DEPARTMENT
BERKELEY, CALIFORNIA 94720